Resistive electronic skin

3 authors, including:

Naveen Noah Jason
Monash University (Australia)
9 PUBLICATIONS **686** CITATIONS

Some of the authors of this publication are also working on these related projects:

Resistive Electronic Skin View project

REVIEW

Check for updates

Resistive electronic skin

Naveen N. Jason, My D. Ho and Wenlong Cheng *

Devices made from traditional conductive bulk materials using complex microfabrication methods often are restricted to being rigid and in some cases, flexible but not strethcable. The main reason is the mismatching mechanics between these traditional materials and the elastomeric materials they were bonded with, which causes materials delimination and/or cracks at soft/hard materials interfaces under strains. Conductive nanomaterials potentially offer new opportunity to tackle this challenge. Their availability in various sizes and shapes enables us to create composites with various dimensions, such as 1D conductive traces, 2D film, and 3D sponge-like architectures. These have opened the door for fabrication of stretchable interconnects, circuits, energy storage devices, antennas, LEDs, etc. The basis of using conductive nanomaterials composites in sensors is that any stimulus or change will generate a measurable electrical impulse. These impulses can be broadly classified as piezoelectric, triboelectric, capacitive, and resistive responses. Depending on the sensitivity required and the preference of electrical impulse to be measured, the device construction maybe tailored to give one of the four kinds of electrical responses. Resistive sensors in addition to being the easiest to construct are also the easiest to measure, which is the crucial reason for a large number of publications in this area. The working mechanism of resistive sensors based on the constituent conductive materials and their percolation network will be discussed in detail. Composition of conductive inks fabricated using wet chemistry methods, and nanomaterials using dry methods, their subsequent applications are covered as well. The exciting applications relating to human health and well-being will also be described. Finally a brief outlook of the future of wearable sensors as "invisibles" will be presented.

1. Introduction

Innovative use of conductive nanomaterials as inks and paints has greatly simplified the fabrication of soft electronic devices.

Department of Chemical Engineering, Faculty of Engineering, Monash University, Clayton 3800, Victoria, Australia. E-mail: wenlong.cheng@monash.edu

Naveen Noah Jason is a PhD candidate, under the supervision of Prof. Wenlong Cheng at Monash University, Australia. He received his Bachelor of Technology in Chemical Engineering degree from Indira Gandhi University of Technology, Sarang, under the Biju Patnaik University of Technology, Rourkela (India), umbrella in 2009. He completed his Masters of Technology (Research) in Chemical Engineering, from the National Institute of Technology, Rourkela

Naveen N. Jason

(India). He commenced his PhD at Monash University in 2013. His research interests mainly involve the development of Electronic-Skin based biomonitoring devices for medical and sporting applications, related to proprioceptive data collection.

My Duyen Ho is currently a PhD candidate in Chemical Engineering Department, Monash University, Australia. Presently, she is working on the projects of stretchable electronic devices and their applications of wearable stretchable sensors. Her work is basically based on 1D-nanowire materials such as silver nanowires and gold nanowires and solution approaches. Previously, she received her Master in Chemical Engineering, Sungkyunkwan University, Korea

My D. Ho

and her Bachelor in the University of Science, Vietnam. Her previous research is mainly related to 0D-nanoparticles, solution processes and their applications on quantum dots light-emitting-diodes.

This combined with printing, weaving, and roll-to-roll processes has enabled soft electronics to become a reality. The growing demand for skin conformable and human interfacing sensors and devices, has promoted new substrates such as rubbers and plastics being embraced. Fabrication of electronics on such stretchable and deformable substrates brings new challenges in terms of conducting materials that stretch. Using nanomaterial inks based stretching percolation networks, as opposed to traditional rigid continuous metal strips/lines is a good solution. This is a logical direction, as much of the large-scale, non-contact, roll-to-roll[1–5] processes such as printing and weaving[6–10] technologies could easily assimilate the new-age conductive inks, paints, and fibres in their systems. This is very advantageous for making the end product economical to manufacture and scale-up. This facile approach for making sensors allows for the sensors to be customizable for a wide range of applications, such as biomedical and sporting devices.

The required conductive nanomaterials can be consisting of various shaped particles of different dimensions; nanoparticles (NPs) – zero dimensional (0D), nanowires (NWs)/nanotubes (NTs) – one dimensional (1D), and micro/nano flakes – two dimensional (2D).[11] For ink based applications they may be suspended in an aqueous or organic carrier fluid based on the method of ink delivery and the substrate characteristics. Subsequently, using the numerous available methods, such as spray coating,[12–16] brush painting,[17–20] pen writing,[21–24] ink-jet printing,[25–28] and Meyer-rod coating,[29–31] they can be applied to the target substrates.[32] Similarly for dry methods, the nanomaterials are usually grown onto substrates using a CVD based method, thereafter they are either woven or transferred onto the target substrate.

Apart from the conductive ink, the substrate on which the ink is deposited also plays a very important role in the device's final performance. Generally using plastics like poly(ethylene terephthalate) (PET), or poly(ethylene naphthalate) (PEN) are used to make flexible sensors for bendable electronics. But if
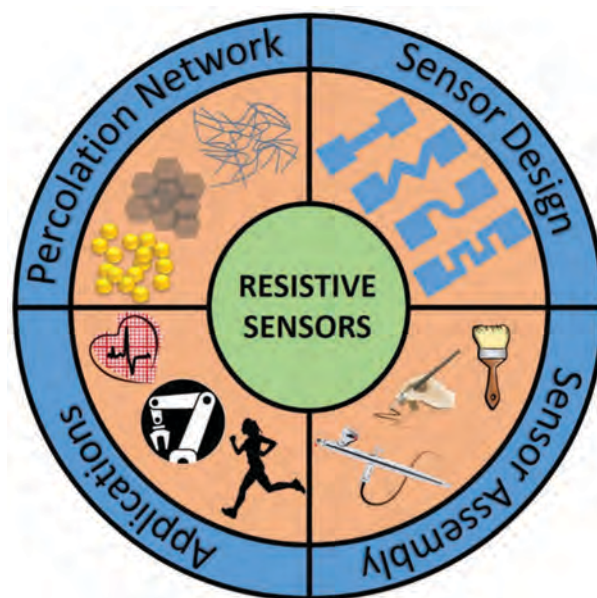

Fig. 1 Schematic showing the key components required to be considered to manufacture a resistive sensor.

the same material is made ultra-thin it maybe cleverly used for stretchable electronics by using a second layer of pre-stretched elastomeric substrates. Flexible substrates are more geared towards developing transparent electrodes for solar cells and display devices. Sometimes using island-device architectures, traditional silicon devices are integrated on flexible islands of plastic, which are strategically shaped to have an unravelling spring like affect when stretched. If the device demands stretchability, then it is best to use an elastomeric substrate such as polydimethoxysilane (PDMS), polyurethane (PU), latex, etc. The beginning of the stretchable sensor boom saw a lot of simple rectangular conductive nanomaterial patch based designs. This slowly graduated to sensor patch embedded bandages, and now most recently complex 1D and 2D fractal designs. Fractal designs greatly enhance the strain range of the sensors. This is done via careful designing so as to ensure that the bulk of the strain is spent on unravelling the fractal coils, and to minimise the strain that is experienced and keep it well below the ultimate strain limit of the substrate. This design allows even rigid and brittle materials such as silicon to be woven into springs. An elastomer with the same design will have significantly more range than its silicon counterpart.

The final device is made by assembling the ink and the substrates together. Primarily, the sensors fabricated till date can be categorized into strain,[33,34] pressure, temperature and chemical sensors. All of these functions can be achieved by designing the substrate appropriately and choosing a nanomaterial ink that suits the application. The material properties of a sensor can be studied by studying the ink, its components and the substrate. Whereas, the electrical properties of a sensor can be studied by assembling the components into transduction devices broadly as a piezoelectric, triboelectric, capacitive, or a resistive device.
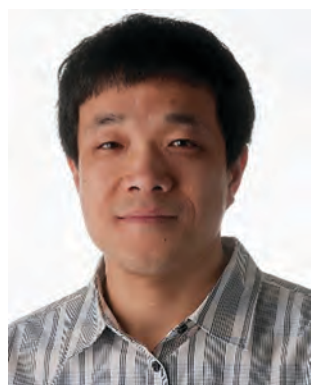
Wenlong Cheng

Wenlong Cheng is a professor and director of research in the Department of Chemical Engineering at Monash University, Australia. He is also an Ambassador Tech Fellow in Melbourne Centre for Nanofabrication. He earned his PhD from Chinese Academy of Sciences in 2005 and his BS from Jilin University, China in 1999. He held positions in the Max Planck Institute of Microstructure Physics and the Department of Biological and Environmental Engineering of Cornell University before joining the Monash University in 2010. His research interest lies at the Nano-Bio Interface, particularly plasmonic nanomaterials, DNA nanotechnology, nanoparticle anticancer theranostics and electronic skins.

Piezoelectric materials as transducers were the material of choice to detect primarily pressure or material deformation based stimuli a decade ago.[35] Recently their role has shifted to be used more as nano-generators to generate electricity *via* a flexible device. Piezoelectric materials have not seen much use in E-skin based applications due to their fundamental drawback of not being able to detect static and sustained stimuli.[8,36–38] This is because the polarisation of charges in a piezoelectric material is dependent on dynamic deformation based stimuli. This polarisation gives rise to a detectable electrical potential. On ceasing the deformation the charge production also stops, and therefore there is no detection even though there is a sustained stimuli. This problem is not faced by resistive sensors as they simply reflect the current state of the stimuli, *e.g.* a sustained pressure will register a continuous high resistance signal, whereas a dynamic pressure input will be reflected accordingly. Recently a flexible sensor with static touch and dynamic touch and temperature sensitivity was developed.[36] They utilised PVDF for the dynamic touch and temperature stimuli, but they circumvented the unavailability of static touch by using reduced graphene oxide as the resistive material. Apart from signal generation problems, piezoelectric devices also don't translate well as flexible devices. Most piezoelectric materials are crystalline, excepting a few popular polymers such as PVDF.[8] ZnO NWs can be used to make flexible and stretchable piezoelectric sensors as well, but presently most piezoelectric materials applications have been focussed on triboelectric power generators. Interestingly, some piezoelectric materials such as ZnO NWs,[39] GaN NWs,[40] and InN NWs[41] also show conducting properties, enabling their uses as resistive sensors as well.[39] There have also been innovative use of biomaterials such as fish scales as a piezoelectric power generator.[42]

The triboelectric effect is a build-up charge on surface of a material when it interacts with a material with significantly different triboelectric potential than itself. This interaction is primarily contact–separation–contact, sliding, or friction based. The built up charge can be discharged through a circuit to power a device or detect a stimuli. Zhong Lin Wang's group has developed a number of self-powered sensors based on this concept, but they are more focussed on the energy generation aspect of the device.[43] A triboelectric device being a double plate device similar to the construction of a capacitor has inspired Zhenan Bao's group to come up with a pressure, bending, stretching responsive capacitive sensing and a triboelectric energy harvesting device.[44] This is possible because of the micropore air gap PDMS layer used as a dielectric in the device which can promote contact electrification between the more electronegative oxygen plasma treated PDMS and the two SWNT coated layers. This is an innovative method that takes advantage of the device architecture to incorporate multiple signal transduction mechanisms such as, capacitance and triboelectricity using the same materials.

Capacitive sensing on the other hand is similar in construction to triboelectric devices in terms of the double plate architecture. But it is different in function, as upon stimuli it doesn't generate an electric potential by itself; like a piezoelectric

device, or by its construction or design; like a triboelectric device. A certain voltage is applied to it and this charge can be stored as potential difference in a capacitive device. This capacitance of the device can be varied by change in the surface area of the plates, the distance between the plates, or both together. This is achieved in an E-skin device by stretching, pressure, torsion, *etc.*, all of which affect the capacitance by varying the plate area and distance.[45] The advantage of capacitive sensors is that as the surface charge of a plate can be easily influenced by another object's surface charge it can sense very close approaching objects, without actual touch. It is also very sensitive to pressure due to very tiny changes in the plate area and distance parameters. The sensitivity may be increased with microstructuring the conductive plate surface in order to have a variable dielectric.[46] The disadvantage being the complicated double layer structure with a dielectric layer in between which thickened the device. This may also have an effect on the stretchability of the device.

A resistive device in comparison to all the above mentioned device operates on a much simpler mechanism, which is the increase or decrease of electron flow pathways through an electrically conductive material when subjected to the stimuli described earlier. It is also facile in construction, as it has only a single layer as the sensing layer with electrical leads from both ends. The ease of measurement of electrical signals, coupled with the simplicity of its construction has made resistive sensors one of the most studied sensors. This motivates the development of this review on resistive sensors. The percolation networks formed by conductive ink components, working mechanism, ink characterization, performance evaluation of the sensors, and the applications of the sensors are covered in further sections.

2. Design principles

2.1. Percolation based mechanism

2.1.1. Percolation networks from 0D, 1D, 2D materials. There are essentially three types of shapes of conductive materials which may be used for the purpose of making a sensor; 0D – zero dimensional, nanoparticles (NPs), 1D – one dimensional, nanowires (NWs), nanotubes (NTs), 2D – two dimensional, micro-nano flakes or platelets. These materials are either used as a filler material in a conductive composite, or as a coating, film, and ink trace. In either state it is required that the conductive elements make contact with each other and provide a pathway for electrons to flow. The point when the percolation network is established can be determined using the volume fraction of the conductive fillers in the composite matrix using the following equation:

$$\sigma = \sigma_0 (V_F - V_C)^s \qquad (1)$$

With "σ" and "σ_0" being the electrical conductivity of the composite matrix and the conductive filler respectively, "V_F" and "V_C" being the volume fraction of the filler at present and the one required for establishing percolation threshold, and "s" being the critical exponent of conductivity. As the final conductivity depends on a lot of variables such as, particle

diameter, length, aspect ratio, distribution, and most importantly inter-particle distance. The value of "s" varies greatly according to these parameters. It ranges from approximately 1.3 for particles,[47,48] 1–10 for nanowires and nanotubes[49,50] and 2 for flakes and platelet.[51,52] Based on a simple model relying on inter-particle distance Kim *et al.* have suggested an efficient method to predict the percolation threshold for 0D, 1D and 2D conductive particles in a polymer composite. In this model, there is either complete physical contact between the particles without any contact resistance, or an incomplete contact which establishes a tunnelling resistance for an electron flow. This tunnelling resistance is inversely proportional to the inter-particle distance. Now, assuming that each particle is in a cubic cell and oriented randomly; Fig. 2(a, b, c) for 0D, 1D, 2D particles, the percolation threshold may be regarded as the average inter-particle distance at which effective electron tunnelling occurs. This required volume fraction may be described by the following equations:

$$V_{0D} = \frac{\pi D^3}{6(D + D_{IP})^3} \quad (2)$$

$$V_{1D} = \frac{\xi \varepsilon \left(\frac{\pi D^3}{6} \right)}{(D + D_{IP})^3} + \frac{(1-\xi)27\pi D^2 l}{4(l + D_{IP})^3} \approx \frac{\xi \varepsilon \pi}{6} + \frac{(1-\xi)27\pi D^2}{4l^2} \quad (3)$$

$$V_{2D} = \frac{27\pi D^2 t}{4(D + D_{IP})^3} \quad (4)$$

$$R_{tunnel} = \frac{E}{AJ} = \frac{h^2}{Ae^2 \sqrt{2m\lambda}} \exp\left(\frac{4\pi d}{h} \sqrt{2m\lambda} \right) \quad (5)$$

Here "D" represents the diameter for particles, diameter of cross-section for nanowires and nanotubes, and diameter of the lateral surface for flakes and platelets. D_{IP} represents equal to

or less than inter-particle distance required for electron tunnelling and for practical purposes is taken as 10 nm for most cases. The thickness of the 2D particle is given by "t". The 1D particles have a more complex interaction in the composite matrix. In most cases, not all of the NWs/NTs are dispersed as separate particles. A significant fraction of the total population of NWs/NTs exist as entangled bundles. Therefore to account for them, the variables "ξ", the volume fraction of the bundles, and "ε", the volume of the bundles are introduced in the equation as well. The tunnelling resistance between two adjacent conductive nanoparticles can be estimated by the eqn (5) by Simmon's theory. "R_{tunnel}" represents the tunnelling resistance, "E" the electrical potential difference, "J" the tunnelling current density, "A" the cross-sectional area of the tunnelling junction, "d" the distance between adjacent NPs, "h" Plank's constant, "m" the mass of an electron, and "e" its charge, "λ" the height of energy barrier for the polymer matrix.

The realistic example of percolation networks formation can be seen in Fig. 2(d–f) for gold nanoparticles (AuNPs),[54] silver nanowires (AgNWs),[34] and graphite nanoplatelets (GrNPls).[55] Using the equations the volume fractions required for each kind of particle can be easily estimated. Kim *et al.* predict that the percolation network and the diameter of a nearly spherical particle have a linear relationship.[56] Therefore, if the particle diameter is sufficiently large enough ≥ 1 μm, to overcome the minimum interparticle distance, the required percolation stabilizes at 50 vol%. A nanoparticle < 50 nm diameter however will require a much lower volume fraction; $V_{0D} \approx 2.5$ vol% for 10 nm NPs. But for the sake of increasing electrical conductivity and viscosity much higher concentrations are used for inks.[57] 2D and 1D particles on the other hand have an inverse relationship with the volume fraction for percolation threshold. Increase in the diameter and decrease in the thickness of a 2D particle lowers the V_{2D}.[58] Specifically, with a thickness "t" of less than 10 nm and a diameter larger than 10 μm *i.e.* aspect ratio > 1000, the $V_{2D} < 1$ vol%.[56] Similarly, 1D particles with an aspect ratio > 1000 can have a $V_{1D} \approx 0.01$, and with a greater aspect ratio the D_{IP} becomes negligible. Even so, the V_{1D} can be driven up if the NWs/NTs bundle volume is found to be $\xi \leq 4$. For the D_{IP} to be negligible the $\xi \approx 0.01$.[59] At this stage, this estimation for the particles' percolation threshold is sufficient, but for a realistic application parameters such as the interaction and bonding with the composite polymer, the effect of a size distribution will also need to be accounted for.[50]

2.1.2. Material basis. The theory of percolation thoroughly discussed nanoparticles of all dimensions; 0D, 1D, 2D, and this applies to nanoparticles of all conductive materials. Hence, this section will focus on the percolation networks formed by the other spectrum of conductive materials, *i.e.* conductive polymers, inorganic oxides and its various morphologies, and finally hybrid conductive materials.

2.1.2.1 Conductive polymers. There are a number of other alternatives which apart from purely to designing conductive resistive materials other than strictly using singular conductive fillers and relying on their percolation networks for sensitivity,
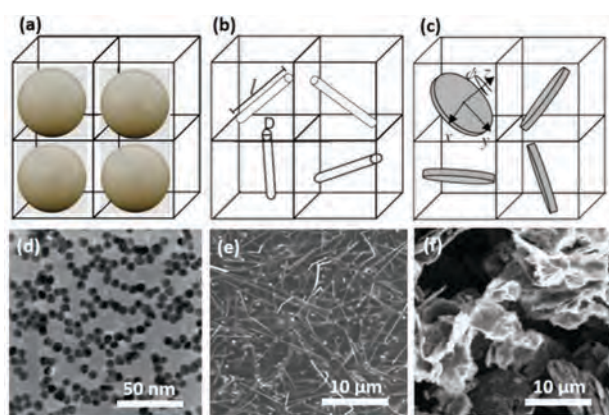

Fig. 2 Influence of (a) 0D,[53] (b) 1D,[53] and (c) 2D,[53] conductive fillers on the percolation network formed in a conductive composite, *Nano Today*, **9**, 244–260. Copyright (2014), with permission from Elsevier.[53] (d) AuNPs, *Nature*, **500**, 59–63, Copyright (2013), with permission from Nature,[54] (e) AgNWs, *ACS Nano*, **8**, 5154–5163, Copyright (2014), with permission from American Chemical Society,[34] (f) GrNPls, *Sensors*, **10**, 3597–3610, Copyright (2010), with permission from Multidisciplinary Digital Publishing Institute.[55]

as describe in the previous sections. Before the existence of flexible and stretchable conductive filler based filler materials, electronics was solely reliant on rigid semiconductor materials. The introduction of conductive polymers created a revolution in terms of flexible and stretchable, plastic electronics.[60,61] Some organic polymers such as polyaniline can be doped from its insulator or semiconductor state, like glass or diamond, all the way to metallic state, like silver or copper. Poly(3-hexylthiophene) (P3HT) can even be turned superconductive when in a super-cooled state. These changes in conductivity are achieved by doping. The percolation network exists at a molecular level for these polymers. Electric current can flow either by electron or hole hopping on the π electron system of the polymer backbone, in redox reaction doped n-type[62–64] or p-type[62,63,65] conductors, or by flow of ions which are formed by rearranging the energy levels through non-redox doping. As the range of conductivity extends from semiconductor or insulator state to metallic conductor state, a resistive sensor may be designed by using just the conducting polymer with various amounts of doping according to the application. If the mechanical and electrical properties do not correspond to the sensor needs, then a conductive polymer may be blended with a suitable mechanically complaint polymer to reap the best of both. This will be the key step in realizing truly stretchable conducting polymers for resistive and other types of sensors, as shown in Fig. 3(a).[66–70]

Recently, organic salts have been used as ionic liquids (IL) which have been used in sensor.[72] The ionic liquid is usually either mixed as a component of a composite, or is used as a medium to disperse CNTs.[73] In this organic salt, one or both ions may have a delocalised charge, and as one of the components is organic the salt can't form a crystal lattice and stays as a liquid. Due to its liquid form, the IL will have a low young's modulus; <1 Pa, and therefore can be pumped into

channels in an ecolfex band which has a young's modulus between 1–100 MPa. Typically, conductive fillers have a young's modulus of over several GPa, which is the root of the fundamental material mismatch problem in a composite material conductor/sensor. The use of ILs allows for a virtually fatigue free, easily mouldable sensor which can be easily manufactured using a "fill and seal" strategy.[72]

2.1.2.2 Inorganic oxides. Although transparent conducting oxides (TCOs) have existed for over a century now, but it was only with the launch of touch based smartphones and tablet devices that the market for them has truly exploded. A large volume of all the TCOs being produced were used for the brittle and rigid glass based touchscreens. Therefore much of the research in that era till before the early 2000s has been dedicated to manufacture large area TCOs electrodes using methods such as sputtering, spray pyrolysis, chemical vapour deposition (CVD) *etc.*[74] In a film state TCOs have a similar percolation mechanism as conductive polymers. Doping is used to give rise to n-type and p-type conductors; ITO being the most popular n-type TCO. The primary method for giving rise to donor ions in n-type TCOs is through doping ions, oxygen vacancies, and interstitial metal ion impurities. With the rise of flexible and stretchable devices the focus is shifted towards fabrication of TCOs based inks which have NPs and NWs/NTs as the conductive elements, ranging from zinc oxide (ZnO), zinc doped aluminium, gallium, indium oxide (AZO, GZO, IZO), tin doped indium oxide (ITO) *etc.*, as shown in Fig. 3(b).[71] These inks can be easily integrated into the existing batch processing and roll-to-roll processes and pave the way for completely transparent electronics.[74] As the inks are composed of nanoparticles, therefore they follow the same percolation network principles as explained earlier for 0D, 1D, 2D particles.[75,76]

2.1.2.3 Hybrid percolation networks using multiple materials. Apart from the standard percolation networks that have been covered so far, there are also hybrid percolation networks created by blending conductive polymers with metal NPs, or mixing 0D, 1D, and 2D particles together,[77–80] or by making a polymer conductive by generating metal NPs *in situ.* By simple mixing of polyaniline (PANI) microparticles (MPs) with AuNWs a hybrid percolation network of 0D and 1D particles was established, as shown in Fig. 4(a).[81] If the resultant ink trace formed a continuous film of PANI, with AuNWs uniformly dispersed in it then we would see enhancement of conduction of electrons. Any gaps or tunnelling resistance between improperly contacting NWs would be seamlessly bridged by the PANI film's molecular π-system percolation network. But this film suffers from non-stretchability as PANI is not a very stretchable polymer even as MPs, as proven by our work using a blend of just 20% (w/w) of PANI with the AuNWs each having the same concentration by weight. Therefore use of PANI even as MPs was limited to 10% to allow for stretchability of the hybrid film. The role of PANI MPs thus is limited to providing pliable MPs at the locations of contact resistance, and enhancing tunnelling between the AuNWs, as shown in Fig. 4(d).
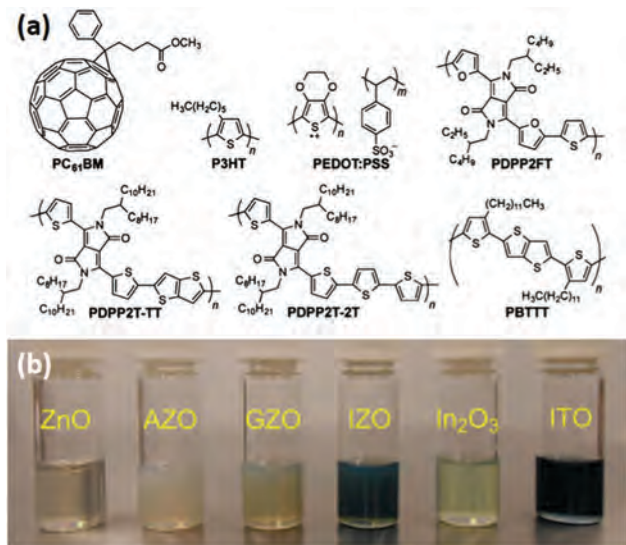

Fig. 3 Conductive alternatives (a) conducting polymers, *Chem. Mater.*, **26**, 3028–3041, Copyright (2014), with permission from American Chemical Society,[66] (b) conductive oxide inks, *Angew. Chem., Int. Ed.*, **54**, 462–466, Copyright (2015), with permission from John Wiley and Sons.[71]
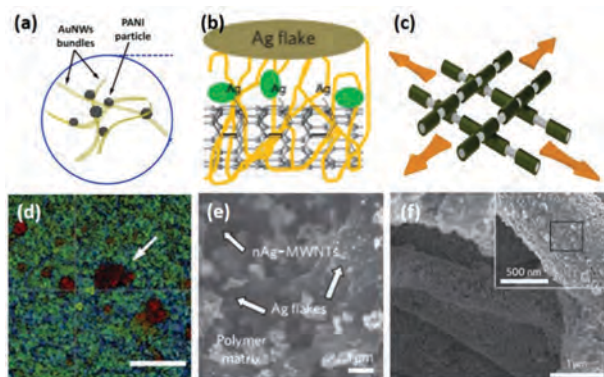
Fig. 4 (a) Conductive polymer–metal NPs composite, PANI–AuNWs, *ACS Appl. Mater. Interfaces*, **7**, 19700–19708, Copyright (2015), with permission from American Chemical Society,[81] (b) 0D–1D–2D, AgMF–AgNP–CNTs polymer composite, *Nat. Nanotechnol.*, **5**, 853–857, Copyright (2010), with permission from Nature,[73] (c) AgNPs *in situ* synthesis in SBS rubber, *Nat. Nanotechnol.*, **7**, 803–809, Copyright (2012), with permission from Nature.[6] (d) The optical microscopy image of the AuNWs–PANI MPs composite, (e) the SEM image of the AgNPs–CNTs–AgMFs composite, (f) the SEM image of the AgNPs–SBS fibre composite.

In Fig. 4(b) we can see AgNPs decorated CNTs which were mixed with a pyridinium based ionic liquid to form a gel. This gel was mixed with Ag flakes in a PVDF copolymer solution, which was then cast and cured to give the final product, seen in Fig. 4(e). This composite consists of AgNPs-0D, CNTs-1D, Ag flakes-2D particles, ionic liquid, and PVDF a piezoelectric polymer. This essentially is a mix of almost all the classes of conductive materials in one composite, which obviously gave rise to a high conductivity of 5710 S cm^{-1}. With so many materials it becomes even more important to carefully tune the concentrations of the fillers so as to prevent the film from becoming brittle and rigid. The resultant percolation network is unchanged in conductivity when subjected to almost 100% strain. At this point, the resistance of a piece of this composite becomes simply a function of strain and the Poisson's ratio. It was observed that the conductivity fell significantly at high strains, which is a drawback in terms of practical applications. This could be solved by using a polymer which had a higher Poisson's ratio. In addition, there is also the problem of phase separation of the conductive fillers after long term repeated stretching. This may be solved by optimising the conductive filler concentrations. A detailed description of the 3D percolation theory is available in the literature.[73]

Growing conductive fillers within the elastomer itself is an excellent method to create a stretchable conductor/sensor. This eliminates the problem of mixing the conductive filler and the elastomer properly to ensure uniform distribution throughout the volume and surface area of the resultant composite. The problem of incompatible solvents of the conductive filler and the polymer is also eliminated. The only drawback of this method being that currently this method is limited to synthesizing only metal NPs *in situ*.[6] The 0D particle percolation network achieved here is close to ideal. It gives us maximum particle loading with uniformity of distribution. Fig. 4(c) shows

the schematic for the resultant conductive rubber fibre mat in a stretched position.[6] Poly(styrene-*block*-butadiene-*block*-styrene) (SBS) is electro-spun into a fibre mat. On this mat the AgNPs precursor (AgCF3COO) in ethanol, is patterned by spray painting, inkjet printing, and nozzle printing. For the purpose of making a strain sensor the mat is also completely soaked in the AgNPs precursor solution till it swells. This infiltrated mat is later subjected to reduction *via* a hydrazine hydrate solution to produce the AgNPs, giving a conductivity of $\sigma \approx 2200$ S cm^{-1} at 100% strain. The percolation network of the AgNPs extends both within and on the surface of the fibres as shown in Fig. 4(f).

2.2. Crack based mechanism

After a thorough discussion regarding the formation and functioning of various percolation networks, it is required that we understand the mechanism that causes changes in its morphology through manipulation of the conductive fillers, when under strain, pressure, shear, and torsion based stimuli. Some studies claim that the change in the resistance reading of a resistive sensor subject to stimuli, is due to bottle neck formations in the conductive fillers network or simply because of contact resistance arising due to reorientation of the same.[34,82] Further studies have shown that these changes occur due to crack and tear formation in the conductive filler network. As 0D, 1D, and 2D fillers have different dimensions, they will likewise be influenced differently,[83] as shown in Fig. 5(a) for AgNPs,[84] Fig. 5(b) for graphene MFs,[85] and Fig. 5(c) for AuNWs.[81] Wagner *et al.* show in their work that a continuous thin gold film can only stretch for 1–2% without plastic deformation. However, the same plastic film adhered to an elastomeric substrate sustains micro-cracks while being stretched to almost 30% strain elastically.[88–90] This behaviour was attributed to two factors. The first being, a compliant elastomeric substrate to which the thin film is bonded, which allows for micro-crack formation, and out of plane twisting and deflection of the film at the crack site. The second being, the formation of micro-cracks which allow for formation of a percolation network and elastic elongation of the thin film, while minimising the effective strain experienced by it. Hence, even on applying a large strain on the thin film–elastomer composite only a small effective elastic strain is experienced by the metal thin film. This also minimize further elongation of the crack as less energy is accumulated at the crack tips, which is released by crack elongation while enduring strain.

On subjecting a conductive film to extended durations of cyclic tests lateral cracks parallel to the direction of strain develop apart from the transverse cracks developed earlier due to the Poisson effect.[87,91,92] The crack microstructure gradually evolves to a conductive island matrix, as shown in Fig. 5(d). On application of low amount of strain the electric current flows through the percolation network which is a higher resistance path than through the intact film, as shown in the middle image of Fig. 5(d). On increasing the strain the islands are pushed together due to transverse compressional stress due to strain in the perpendicular direction. This provides a more direct lower resistance pathway for electron flow, as shown in the last image in Fig. 5(d). These changes in the percolation network are reflected in the electrical resistance
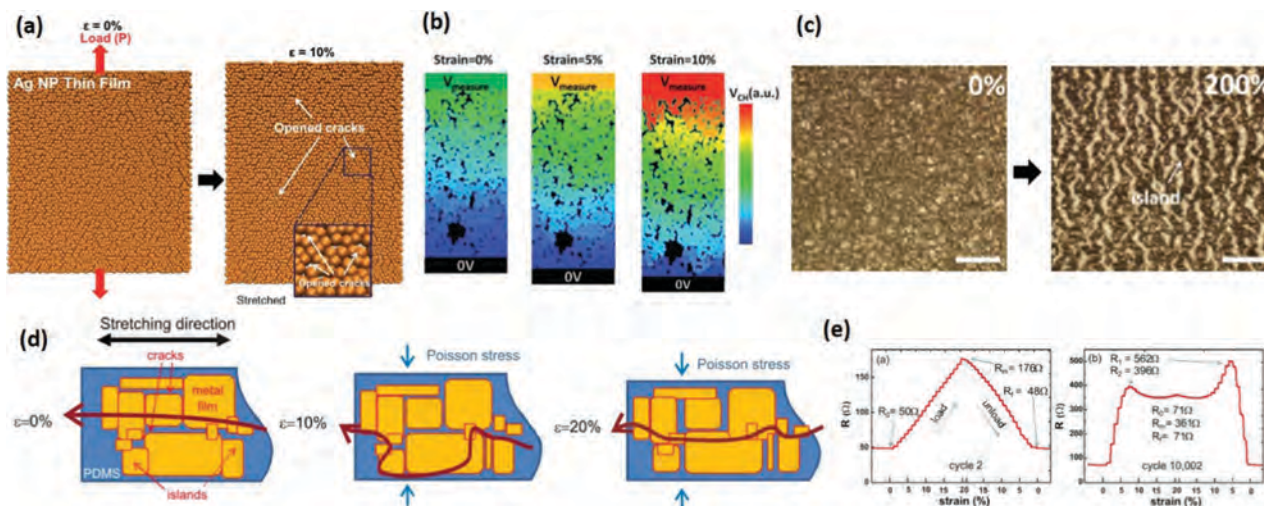
Fig. 5 Crack formation in (a) AgNPs film, *Nanoscale*, **6**, 11932–11939, Copyright (2014), with permission from The Royal Society of Chemistry.[84] (b) Graphene flake film, *Nanoscale*, **6**, 699–705, Copyright(2014), with permission from The Royal Society of Chemistry.[85] (c) AuNWs film, *Adv. Electron. Mater.*, **1**, 1400063, Copyright (2015), with permission from John Wiley and Sons.[86] (d) Percolation network through island network formed after extended cyclic strains, *Appl. Phys. Lett.*, **94**, 71902, Copyright (2009), with permission from American Institute of Physics.[87] (e) Electrical resistance profile at 2 and 10 002 cycles of strain.[87]

profile as well for the stretch–release cycle, as shown in Fig. 5(e). The first image shows a normal peak formation for a stretch–release cycle where there is only transversal cracks in the film. But after 10 000 cycles the profile changes to include two resistance maximas, which correspond to the percolation networks parallel and perpendicular to the strain direction which signifies island network formation.

Recently this phenomenon has been exploited to make a square island matrix which is formed by using guided straight line cracks.[93] Patterned holes are strategically and uniformly distributed on a polyurethane acrylate (PUA) film which has an evaporated chromium and platinum layer as the sensing element. On the application of stimuli the stresses are concentrated near the holes which then force the formation of guided straight line cracks. Being able to control crack formation opens up a new method to be able to control the dependence of resistance on strain. A pressure, strain, and blood pulse sensor was formed using this composite, with extraordinary sensitivities of over 10^5 at a pressure range of 8–9.5 kPa, and a gauge factor of 2×10^6 in the strain range of 0–10%.

Depending on the dimension of the particles the crack and tear mechanism will slightly vary. As the 0D particles are closest to a continuous film, they will experience the formation of an island matrix the most. This percolation network is also expected to rely significantly on tunnelling. The 2D particles on the other hand have a large majority of overlap area between the particles. For graphene, where there is a mechanism for platelet sliding as well, the percolation network will be mostly affected by overlap area and change in contact resistance during strain. However, for a more rigid microflake materials such as graphite[94] or metal flakes the out-of-plane twisting and deflection and subsequent breakage and establishing of electrical contact with other MFs plays a bigger role in influencing the percolation network than tunnelling.[85] Therefore mostly

transversal micro-cracks will be observed upon stretching. In case of 1D particles the aspect ratio is much higher, therefore a single nanowire/nanotube is able to interact with thousands of other NWs/NTs. In such a case NWs reversible sliding and contact resistance again will be the leading contributors to the percolation network, whereas tunnelling will have a minor contribution. The NWs/NTs network will be even less affected by stretching, compared to 0D and 2D particles. Therefore we expect to observe a majority of transversal cracks on the film, and minimum appearance of parallel cracks or island formation, as shown in Fig. 5(c). To design an efficient 1D network, parameters such as the curviness and waviness of the NWs/NTs, its diameter distribution, the compactness of the geometrical shaped voids formed in the network, and the number of dangling and unconnected NWs/NTs, need to be carefully considered.[95–97]

2.3. Self-healing mechanism

The problem of conductive percolation network fatigue endured due to cracking, tearing, and phase separation puts a limit to the lifetime of a sensor.[98] To counter this researchers have come up with self-healing composites which essentially reverse wear and tear and extend the lifetime of the sensor indefinitely.[99] Such self-repairing sensors will have applications in devices which usually undergo constant deformation such as soft robotics and bioprosthetics based. Fig. 6(a) shows an example of 0D Ni MPs based composite. A hydrogen-bonding network based supramolecular polymer is blended with urea functionalized Ni MPs with nanoscale surface roughness, Fig. 6(d).[100] The polymer has a glass transition temperature T_g below room temperature, which allows room temperature bonding. The asperities on the Ni MPs surface promotes wetting by the polymer, while the urea ligand promotes hydrogen bond formation with the polymer. The hydrogen bonds are spontaneously associating and dissociating, which forms the basis for the healing mechanism if there is a cut or
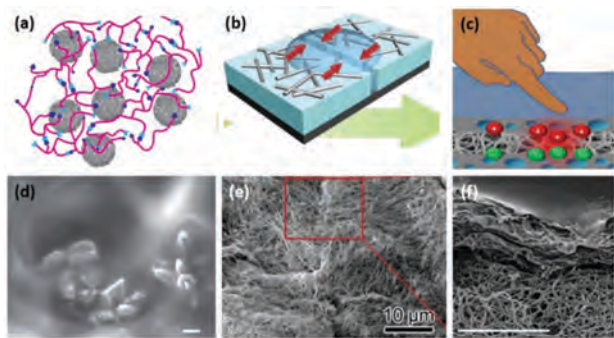
Fig. 6 Dynamically established percolation network in (a) 0D, polymer–Ni NPs, *Nat. Nanotechnol.*, **7**, 825–832, Copyright (2012), with permission from Nature.[100] (b) 1D, AgNWs/(bPEI/PAA–HA), *Adv. Mater.*, **24**, 4578–4582, Copyright (2012), with permission from John Wiley and Sons.[101] (c) PVA– graphene/PVDF/PDMAA, *Sci. Rep.*, **3**, 3138, Copyright (2013), with permission from Nature.[68]

scratch on the polymer. The Ni MPs by being part of this hydrogen bond network provide a tunnelling based percolation network. On being completely cut into separate pieces and put back together with slight pressure, 98% of the original conductivity can be recovered in 15 seconds. Increasing the concentration of the Ni MPs more than 31 vol% (75 wt%) causes loss in mechanical strength and recoverability as there are now not enough polymer molecules in the matrix at the cut interface for hydrogen bonding. There is also an increased chance for phase separation.

Fig. 6(b) shows a 1D Ag NWs based self-healing composite. This composite is fabricated *via* layer-by-layer assembly. Branched poly(ethylenimine) (bPEI) and poly(acrylic acid)–hyaluronic acid (PAA–HA) are blended together and applied as alternating layers with drop-casted poly(vinylpyrrolidone) (PVP) coated Ag NWs, Fig. 6(e). The HA segment of the polymer is highly water absorbent, and makes the composite transparent and flexible. Similar to the earlier case, there is a strong hydrogen bonding interaction between the carboxylic acid groups of the polymer blend and the pyrrolidone groups on the AgNWs. But unlike the previous case, upon getting cut the cut is to be wet with deionized water to kickstart the healing which took 2 minutes to complete. As a control experiment, Ag layers of the same thickness were evaporated and deposited in the composite. Upon cutting, the polymer layer healed after wetting with water, but the Ag layer was permanently damaged. This highlights the importance of having discrete filler particles which can move around and establish new bonds at the cut site interface during healing. This AgNWs–polymer selfhealing also has a high transmittance of 60%, which may be used as self-healing transparent sensors in the future.

The composite in Fig. 6(c) is a 2D conductive material assembly. Here poly(vinyl alcohol) and graphene are turned into a porous foam scaffold, which is infiltrated with poly(*N*,*N*-dimethylacrylamide) (PDMAA), and results in crosslinking of the PDMAA on the 3D graphene network. The PDMAA hydrogel through diffusion gets intimately linked with the graphene scaffold in this way, Fig. 6(f). This composite conductive hydrogel is stretchable, and its self-healing capability relies

on hydrogen bonding just as the previous two cases. As the diffusion of the PDMAA chains and their subsequent establishment of new hydrogen bonds at the cut-site is a slow process, the healing time is about 12 hours at room temperature.

The self-healing conductive composites generally carry discrete conductive fillers, preferably which have a ligand bound to them which can make hydrogen bonds with the polymer matrix. As the polymer chains are bound to each other by hydrogen bonds, there is constant association and dissociation of bonds which allows for "healing" at a cut-site interface. Such a dynamic percolation network will have the ability to spontaneously generate a new electron pathway whenever there is a restriction or resistance due to cuts and scratches on the conductive composite sensor.

3. Device structures and fabrication technologies

3.1. Macroscale patterning

While self-healing is a strategy to repair the percolation network intrinsically, patterning and substrate shape modification is a method which focusses on minimising damage due to strain by introducing designs both at the micro and macro scale to absorb strains.[102–104] This is achieved by introducing spring like deformations through methods such as pre-stretching, using fractal substrate shapes *etc.* in the sensor coating. Much of the strain energy is spent on unravelling the springs, due to which only a small strain which is well below the fracture strain limit of the coating is passed on to the conductive coating.[105–108] The top row in Fig. 7 are examples of nanoscale sensing elements used in a macroscale fabrication, while the bottom row represent microscale sensing elements. In Fig. 7(a) we can observe laterally buckled CNTs on the PDMS surface.[109] This is unlike most coatings, where they undergo out-of-plane buckling when they are placed on a prestretched substrate and then the strain is released. Here, the vertically grown spinable CNTs forests were transferred onto PDMS, after which the PDMS was stretched. This caused the CNTs to slide on the PDMS instead of elongate, as the strain experienced by the CNTs because of the interfacial shear exerted by the PDMS is much lesser than the strain experienced by the PDMS itself. On release of the strain on PDMS, normal stress transfer from the PDMS to the CNTs makes them buckle laterally. These buckles help to absorb strain till they are straightened out, thereafter we start seeing the rise of resistance values. The strain range and responsiveness of a strain sensor may be tuned this way.

In Fig. 7(b), we see the AuNWs ink painted in macroscopic sine wave shapes with varying degree of buckling.[81] We have quantified the wavy patterns using the equation

$$y = A\sin(kx) \qquad (6)$$

where "y" is the contour height of the curve, "x" the length, "A" the amplitude, and "k" the pattern parameter. For "k" being set to 0, $\pi/15$, $2\pi/15$, and $4\pi/15$, the resultant strain ranges obtained were 99.7%, 120.8%, 131.0%, and 149.6%. This could
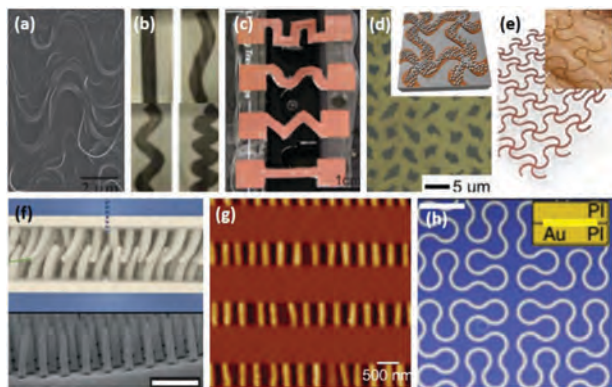
Fig. 7 Macroscale fabrication (a) wavy CNTs, *Adv. Mater.*, **24**, 1073–1077, Copyright (2012), with permission from John Wiley and Sons.[109] (b) Sine-wave patterned AuNWs traces, *Adv. Electron. Mater.*, **1**, 1400063, Copyright (2015), with permission from John Wiley and Sons.[86] (c) CuNWs on shaped elastomeric substrates, *Nanoscale*, **8**, 16596–16605, Copyright (2016), with permission from The Royal Society of Chemistry.[94] Microscale fabrication (d) AuNPs on biaxially stretchable shaped elastomeric substrate *Adv. Mater.*, **23**, 2946–2950, Copyright (2011), with permission from John Wiley and Sons.[110] (e) CuNWs on biaxially stretchable PI substrate, *Adv. Mater.*, **28**, 10257–10265, Copyright (2016), with permission from John Wiley and Sons.[111] (f) Pt coated PDMS micropillars, *Nat. Mater.*, **11**, 795–801, Copyright (2012), with permission from Nature.[112] (g) Rippled graphene ribbons *ACS Nano*, **5**, 3645–3650, Copyright (2011), with permission from American Chemical Society.[113] (h) Fractal curves based Si nanoribbons, *Nat. Commun.*, **5**, 5747, Copyright (2014), with permission from Nature.[114]

be because the shapes with a larger strain range have a larger surface area which allows them to absorb more strain. In addition, the macroscopic curve orientations provided to the AuNWs by means of shear force applied by the Chinese paint brush may be expected to form a macroscale buckling mechanism, similar to the CNTs discussed earlier.

For both the CNTs and the AuNWs cases discussed above the patterns are still on an elastic sheet, and hence are subjected to the deformation on an elastic sheet due to strain,[91] as per the Poisson effect. However, Fig. 7(c) shows CuNWs coated on a free standing shaped substrates. Similar to the AuNWs case, the shapes were quantified on the basis of their length to width ratio, "α". By increasing the aspect ratio of an elastic sheet, the amount of strain experienced by it can be reduced by converting this strain into compressional stress perpendicular to the strain direction. In this way a high "α" sheet can endure a large amount of strain without tearing. One way to increase the effective aspect ratio is to design spring like shapes into the sensor. The four basic shapes explored in this study were the linear, zigzag, serpentine, and square wave patterns, with the linear shape being the control shape. Their respective $\alpha(s)$ being linear – 6.6, zigzag – 8.3, serpentine – 10.6, and square – 14.3. This work has demonstrated CuNWs, GrMFs, and their hybrid percolation network based sensors, the highest strain range reported was 600% for the serpentine shape with the CuNWs coating.

The shape of the substrate also plays an important role in controlling the sensitivity of the sensor. The linear shape behaves as a simple elastic functioning according to the Poisson effect

when subject to strain.[91,105] The zigzag shape however when stretched has large amounts of tensile stress concentrated on the inner sides of the angles, while compressive stress is accumulated on the outer sides of the same angles.[107] This behaviour is also observed in the sharp angles of the square wave shaped substrate. The sharper the angle, the more accumulation of stress. The serpentine shape is generally used to distribute this stress and endure a larger strain. This phenomenon may be used to increase the sensitivity and strain range of a strain sensor by local manipulation of the percolation network.[94] When using a continuous film, strain sensor failure occurs for three reasons. The first being, exerting a strain beyond the ultimate strain of the coating. The second being, the accumulation of stress during cyclic tests, which eventually lead to plastic deformation and subsequent fracture. The third being delamination from the polymer substrate. As a solution to these problems, researchers have started using porous or mesh like conductive films composed of discrete conductive particles. Fig. 7(d) demonstrates a biaxial stretchable zigzag shaped network based on polystyrene substrate with a poly(ethylene glycol) and AgNPs composite coating. The AgNPs were generated *in situ* by reducing its precursor mixed in the PEG polymer. Similarly, Fig. 7(e) is a 1D analogue to the work described in Fig. 7(d). The composite is a serpentine open mesh structure composed of polyimide (PI) and CuNWs. The authors claim that the CuNWs reinforce the mesh structure. The CuNWs themselves can experience a maximum strain of 30%, but as a composite they can reversibly stretch biaxially to 80% strain. These two examples implement the dual strategies of using a fractal mesh to max-imise stretching of the substrate, and using a nanomaterial coating to fabricate a conductive coating with a Young's modulus comparable to the stretchable substrate. The fractal shape brings down the effective strain acting on the structure, while the nanoparticle film has higher resilience to fatigue and cracking. These fractal structures can be designed for enhancing stretchability,[105,115,116] or for efficiently managing area coverage for stretchable devices in island device architectures.[106] One of the most commonly used fractal pattern is the Greek cross, but there are many other curves such as peano, Hilbert, moore *etc.* which may be used in fractal pattern based stretchable electronics.[117] Even if a complex fractal pattern is not used, the elasticity of a structure may be increased by simply increasing the order of the fractal.[105,115,118]

3.2. Microscale patterning

On the microscale,[39,75,119–122] Fig. 7(f) shows Pt coated PDMS micro-pillars which form an interesting percolation network.[112] The structure essentially increases the contact area of the electrodes, and therefore any stimuli measured is in terms of contact resistance. Fig. 7(g) is 2D graphene transferred to a prestretched PDMS substrate, which after strain release resulted in out-of-plane buckling.[113] The change in resistance comes from the scattering of charge carriers during the transition from being non-flat to flat when stretched. The interconnection between nano-graphene domains also contributes to the loss and estab-lishment of percolation networks when under strain and

then release. Fig. 7(h) shows Si micro-ribbons coated with gold in a fractal serpentine shape based fixed electron pathway, instead of a percolation network being used as sensors. The changes in resistance due to stimuli come from the continuous Si ribbon enduring micro-strains.[114] Therefore, the Si micro-ribbons have to be carefully designed so that the remaining strain experienced by it should fall well below its failure/fracture strain after the majority of the strain is spent unravelling the serpentine spring. Hence, depending on the application, shaped substrates,[117] conductive fillers, and microstructures may be arranged into various macro and micro scale configurations.

3.3. Wet chemistry strategy

As most conductive filler nanomaterials are synthesized using wet chemical processes, it is economical to simply use them as inks to minimise the processing steps. Inks also offer the advantage of tailor-made assembly of the sensor using facile methods such as direct writing, spray coating and aerogel formation. Such versatile applications require that the properties of the inks are carefully studied and tuned.

3.3.1.   Ink characterization. Various parameters such as particle dimension, viscosity, conductive filler loading, additives *etc.* need to be considered during ink formulation. Even for the same particle, the parameters would need to be modified depending on the method of ink delivery to the target substrate[123,124] Smooth ink flow appropriate for the delivery method, and the electrical conductivity of the final trace are the two main criteria for the quality of the ink. They heavily depend on the dimensions of the conductive particles, which again decide the viscosity of the ink, and the percolation network formed by the ink trace. Kamyshny *et al.* have gone into great detail in covering these parameters for printing based applications.[125] Fig. 8(a) shows a 1D CuNWs ink, Fig. 8(b) 0D AgNPs ink, and Fig. 8(c) AgNPs and 2D graphene decorated with AgNPs. The CuNWs on average are about 25–35 nm in diameter, and 50–60 μm in length, which gives it a high aspect ratio of 1500–2000. Each CuNW therefore is interacting with 1500–2000 NWs, and this phenomena manifests itself in entanglement issues and clump formation problems. We were able to carefully tune the ink components to achieve a writable conductive ink,[126] which apart from a few CNTs based works[24] hasn't been achieved for metal NWs/NTs. As high aspect ratio 1D conductive fillers can establish percolation network with less material, therefore the ink loading requirement also reduces; only 2 vol% or 18.28 wt% for CuNWs. This is reflected in the concentration required for the viscosity parameter, as shown in Fig. 8(d). The CuNWs solution becomes sludge like at only 2.7 vol%.

A 0D particle based ink requires a concentration of 45–55 wt%, such as for ∼400 nm diameter AgNPs shown in Fig. 8(e), to achieve a similar viscosity of 1–10 Pa s.[57] It is also observed that a high aspect ratio 1D particles have an exponential rise in viscosity, Fig. 8(d), as compared to the 0D particles, Fig. 8(e), which is more linear. This difference in trend is the direct result of the different aspect ratios. Fig. 8(c) shows a hybrid ink; AgNPs 15 wt% and graphene decorated with AgNPs, 0.15 wt%. This ink has high aspect ratio particles as well, owing to
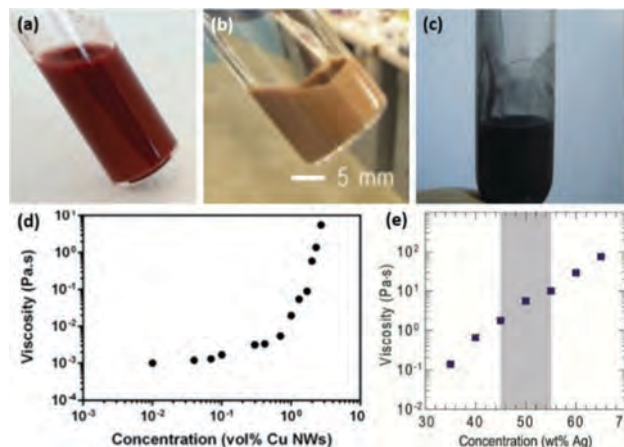

Fig. 8   Conductive inks from (a) 1D CuNWs, *ACS Appl. Mater. Interfaces*, **7**, 16760–16766, Copyright (2015), with permission from American Chemical Society,[126] (b) 0D AgNPs, *Adv. Mater.*, **23**, 3426–3430, Copyright (2011), with permission from John Wiley and Sons,[57] (c) AgNPs and 2D graphene decorated with AgNPs, *Nanotechnology*, **25**, 55201, Copyright (2014), with permission from IOP Science.[127] Viscosity profiles for (d) CuNWs ink, *ACS Appl. Mater. Interfaces*, **7**, 16760–16766, Copyright (2015), with permission from American Chemical Society,[126] (e) AgNPs ink, *Adv. Mater.*, **23**, 3426–3430, Copyright (2011), with permission from John Wiley and Sons.[57]

graphene. However due to the 2D dimension it is expected that there will be a minimum of entanglement and resultant high viscosities as observed with 1D particles. Graphene therefore is expected to have a high viscosity comparable but still less than the 1D particle system. The concentrations required would be similar as well. The main advantage would be the well-connected graphene flake based, overlapping 2D percolation network which can offer high conductivity even with single layers of graphene. A variety of examples of nanomaterials including 0D, 1D, 2D materials, hybrid materials *etc.* and their parameters have been summarised in Table 1.

3.3.2.   1D trace, 2D film, and 3D sponge based architectures in sensor fabrication. In addition to understanding the ink requirements, it is also required that researchers have a good grasp of the various processes used to fabricate 1D, 2D, and 3D composites for the sensor applications. This will be explored in the coming sections.

3.3.2.1 1D conductive trace based sensors. Drawing and writing constitutes a simple yet low-cost strategy to fabricate sensors that are much more personalized and give the end users the freedom to customize them. Also, as there is no need of complex equipment except the user's hands, the process becomes very economical. The brush painting method is basically a capillary device which holds the ink droplets between the brush hairs.[128] When the paintbrush is pressed against the substrate and dragged, the capillary gap is widened to the point that gravity takes over and deposits the ink drops. Based on the thickness of the trace required the paintbrush can be pressed harder to release more ink to get a wider trace and *vice versa*. Establishing a certain electrical conductivity of a trace will require a certain number of layers painted on the same trace, which depends on the viscosity and concentration of the ink.

Table 1 Comparison of 0D, 1D, 2D, and hybrid ink components, concentrations and viscosity required, conductivity achieved, and ink delivery method, specifically used to fabricate resistive sensor

Material	Additives	Concentration	Viscosity	Best trace ohmic resistance	Delivery method	Ref.
0D particles						
AgNPs	Hydroxyethyl cellulose, water, methanol	45–55 wt%	1–10 Pa s	4.34 $\mu\Omega$ cm	Rollerball pen	57
AgNPs	—	20 wt%	15 cP	6.67×10^{-6} Ω m	Spin coating	84
1D particles						
Vapour grown carbon nanofibers (VGCNFs)	Gellan gum biopolymer (GG)	10 mg ml^{-1} VGCNFs, 3 mg ml^{-1} GG	1.1 mPa s	3.4 ± 0.1 kΩ cm	Fountain pen	22
CNTs	SDBS, water	(5 mg CNTs, 10 mg SDBS) per ml in water	—	20 kΩ cm	Fountain pen	130
CuNWs	Hydroxypropyl cellulose (HPC), water	18.28 wt%, 2 vol%	0.6 Pa s	0.85 kΩ	Rollerball pen, brush painting	126
AgNWs	2-Butoxy-1-ethanol, isopropanol, ethanol	15 wt%	13.8 mPa s	12.9 $\mu\Omega$ cm	Drop fit-to-flow	132
2D and Hybrid particles						
Graphite	Clay	9B, 6B, 2B, HB	—	200 kΩ, 500 kΩ, 2 MΩ, 20 MΩ	Pencil drawing	133
AuNWs, PANI microparticles	Ethanol/hexane, 3 : 1 v/v	10 mg ml^{-1} AuNWs, 10 wt% PANI	1.04–44.1 mPa s	148.1 ± 78.2 kΩ	Chinese brush painting	81
AgNPs, graphene–AgNPs composite	Ethanol : ethylene glycol : glycerol = 50 : 45 : 5 vol%	15 wt% AgNPs, graphene–AgNPs 0.15 wt%	—	1.9×10^{-7} Ω m	Rollerball pen	127

As this method requires considerable skill on the part of the end user, the applications may be reduced to simple things such as strain sensor devices.[24,81,126,129] This method has been used successfully for 0D, 1D, and 2D particles based inks, as described below.

The Sydney opera house depicted in Fig. 9(a), used 1D CuNWs ink in the brush painting method to deliver the pattern

Fig. 9 Conductive ink used for making 1D trace using (a) CuNWs-brush painting, *ACS Appl. Mater. Interfaces*, **7**, 16760–16766, Copyright (2015), with permission from American Chemical Society,[126] (b) CNTs-fountain pen writing, *Mater. Res. Bull.*, **50**, 249–253, Copyright (2014), with permission from Elsevier,[130] (c) Carbon black NPs/PDMS-imprinting, *Carbon*, **77**, 199–207, Copyright (2014), with permission from Elsevier.[131] (d) Graphene/AgNPs-rollerball pen writing, *Nanotechnology*, **25**, 55201, Copyright (2014), with permission from IOP Science.[127]

on paper.[126] This complex pattern drawn free-hand is conductive, and this is proven by the glowing LED attached to the circuit. As this is an aqueous ink, therefore there may be slight problems with ink wetting behaviour on interaction with hydrophobic surfaces. But by using a polymer additive, hydroxypropyl cellulose (HPC), the researchers are able to get around this problem and can paint on polyethylene terephthalate (PET) sheets, latex rubber, and various kinds of papers. A bending sensor was drawn on paper, while a strain sensor was painted on latex using the CuNWs ink.

Fig. 9(b) shows an aqueous 1D CNTs ink being deposited by a fountain pen.[22,130] The fountain pen is also a capillary based device, but here the capillary is fixed in a metal nib therefore a more uniform and consistent trace can be obtained. It was also demonstrated that by holding the nib in a fixed spot on paper for 30 seconds, the ink was able to diffuse to the other side of the paper and a continuous conductive circuit could be drawn utilising both sides of the paper. This is an exciting way to replace multilevel architecture based silicon electronics with flexible and environmentally friendly paper electronics.

Fig. 9(c) shows a 0D carbon black NPs and PDMS composite ink, which can be contact-transfer printed on another substrate using micro-patterned PDMS stamps.[131] This study uses photoresist based moulding techniques to make the stamps, but for an industrial scale these may easily be 3D printed as well. Patterns of various lengths and shapes were tested as strain sensors, and they showed highly linear behaviour. The advantage of this method is that it combines the patterning and the stretchable device fabrication into one step. By making an ink which becomes stretchable when cured, much of the post processing work has been eliminated. This technique may be extended to 1D and 2D particles for interesting variations in the strain sensor study results.
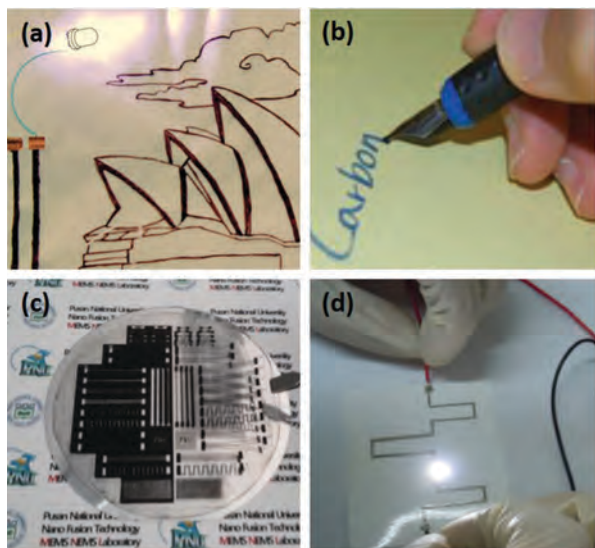
Fig. 9(d) shows a 2D graphene–AgNPs based ink trace being drawn on paper by a rollerball pen.[127] The graphene is decorated with AgNPs to reduce contact resistance between the overlapping graphene flakes. The ink also contains AgNPs by themselves as well. This hybrid ink has been able to cut down the concentration of ink fillers needed to just 15 wt% for AgNPs, and 0.15 wt% for graphene–AgNPs. The hybrid ink takes advantage of 2D graphene, as it doesn't face problems with entanglement and clump formation as the 1D materials. 1D materials also tend to form clogs at the micro gap between the rollerball and the nib sleeve. 2D graphene can act as a lubricant and overcome this problem. The resultant ink trace is expected to be well connected by overlapping graphene layers, which will provide tolerance from stimuli during strain by virtue of their sliding mechanism. Any lack in electrical conductivity is supplemented by the AgNPs resting between and on the graphene. By tweaking the ink components it is possible to fabricate various flexible resistive sensors. Although pen writing use NPs as the conductive fillers of choice in most cases, the previously discussed cases prove that 1D and 2D materials may also be with proper ink fabrication.[24]

3.3.2.2 2D film architecture sensors. Large area sensor applications require that the sensing element be applied uniformly on the whole surface of the target substrate.[134,135] This can be achieved easily by 2D coating methods. Usually the methods used for fabricating transparent electrodes such as spray coating, dip-coating, meyer rod *etc.* can be directly adapted to make a sensor. For instance Fig. 10(a) shows how a CNTs membrane was assembled on a Teflon membrane *via* vacuum filtration, which was later made into a freestanding membrane on water.[136] The pressure sensor is assembled by sandwiching this CNTs membrane between two silk fabric templated micro-structured PDMS sheets, as shown in Fig. 10(d).[137] The micro-structure enhances the pressure sensitivity 2.3 times. Other methods such as dip coating, Fig. 10(b), and spray coating, Fig. 10(c), have also

been used to get a large area film on a PET sheet.[138] Fig. 10(f) also shows that just 3 cycles of dip coating is comparable to 400 times spray coating in terms of sheet resistance and transmittance.[138] This is attributed to the thick bundles based CNTs percolation network, which form a more stable electron pathway while simultaneously allowing for more void spaces on the substrate area. The spray coated network has a more densely distributed percolation network, but it is not as well connected, and also has less void spaces which make it less optically transmissive.

The CNTs films from both methods have been tested for their bending ability, but for the purpose of making a micro-structure based sensor the uniformity of spray coating would be preferred, to ensure uniform sensitivity over the sensor surface area. Spray coating gives a large and uniform area of coverage, but this method also suffers from wastage of the NPs ink, as much of the ink is lost not being sprayed on the targeted area, or ends up on masks used to generate patterns. The Meyer rod technique may be considered as an alternative. Shown in Fig. 10(e), CuNWs were coated on a PET substrate using this technique, and a transparent flexible electrical conductor and bending sensor were fabricated subsequently. This method cannot produce a thin coating like the spray coating method, as the thickness of the ink layer on the substrate is limited by the gap thickness allowed by the Meyer rod, which is usually in the millimetre scale.

3.3.2.3 3D architecture sensors. There are a few methods to make 3D sponges from conductive inks.[140,141] One of the simplest is dip coating, as shown in Fig. 11(a).[142] A piece of tissue paper is dipped into AuNWs ink a number of times and dried. The highly flexible hair like AuNWs being of nanoscale, wrap around the paper's cellulose microscale fibers which act as a scaffold. This porous scaffold provides the basis for a reversible pressure sensing material. This AuNWs infused tissue paper is sandwiched between two PDMS sheets, one of which has evaporated gold interdigitated electrodes. On subjecting this sandwich to pressure, the gap between the electrodes is bridged by the pressure induced
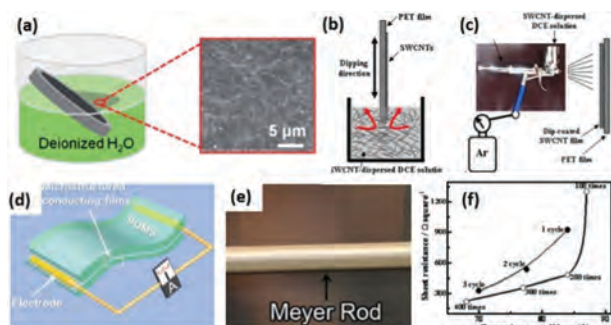

Fig. 10 2D film coating by (a) CNTs film membrane transfer, *J. Mater. Chem.,* **22**, 21824, Copyright (2012), reproduced from ref. 136 with permission from the Royal Society of Chemistry.[136] (b) CNTS dip-coating, *J. Colloid Interface Sci.,* **318**, 365–371, Copyright (2008), with permission from Elsevier.[138] (c) CNTs spray coating.[138] (d) CNTs film in pressure sensor *Adv. Mater.,* **26**, 1336–1342, Copyright (2014), with permission from John Wiley and Sons.[137] (e) CuNWs meyer rod coating, *Adv. Mater.,* **23**, 4798–4803, Copyright (2011), with permission from John Wiley and Sons.[139] (f) CNTs dip-coating and spray coating sheet resistance comparison.[138]
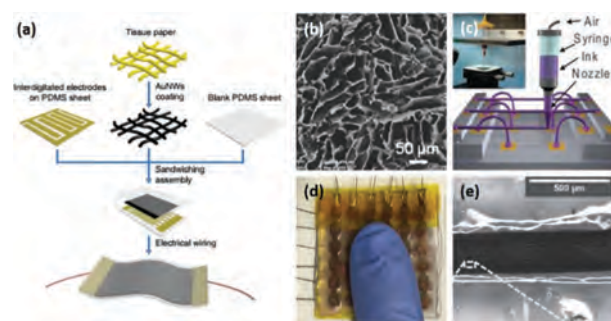

Fig. 11 (a) AuNWs-tissue paper dip-coating, *Nat. Commun.,* **5**, 3132–3140, Copyright (2014), with permission from Nature.[142] (b) AgNWs ice templated foam, *Angew. Chem., Int. Ed.,* **53**, 4561–4566, Copyright (2014), with permission from John Wiley and Sons.[143] (c) AgNPs extrusion *Science,* **323**, 1590–1593, Copyright (2009), with permission from Science.[144] (d) CuNWs aerogel, *Sci. Bull.,* **61**, 1624–1630, Copyright (2016), with permission from Science.[145] (e) CNTs–gellan gum extrusion, *Adv. Funct. Mater.,* **22**, 4790–4800, Copyright (2012), with permission from John Wiley and Sons.[146]

variable resistive composite, and pressure can then be quantified with resistance values. The sensor is sensitive enough to sense blood pulses in the wrist.

Fig. 11(b) on the other hand describes an ice templated AgNWs foam, which naturally has honeycomb shaped pores.[143] This foam is infiltrated with PDMS, and this gives us a strain sensor, which is almost insensitive to bending. As the honeycomb structure is excellent at absorbing and distributing forces acting on it, the AgNWs and PDMS composite is expected to be able to endure extensive cyclic strains and bends. Fig. 11(d) is also an aerogel, like the earlier case. Here CuNWs and poly(vinyl alcohol), (PVA) are used to form the aerogel, but unlike earlier it is not infiltrated by an elastomer.[145] Instead, an Ecoflex framework with a cylindrical chamber for the aerogel is used. This setup was used to make a pressure mapping sensor. The ecoflex framework, in addition to provide the matrix for the pixels, also gave support to the fragile and sensitive aerogels by absorbing most of the pressure input.

Extrusion printing offers an interesting pathway to print circuits in 3D space, as shown in Fig. 11(c) using AgNPs,[144] or by extruding circuits and sensors on absorbing substrates, as shown in Fig. 11(e) using CNTs and gelan gum (GG); a biopolymer.[146] While the AgNPs spanning microelectrodes are almost completely made up metal, they are used as stretchable micro-spring like conductors. Whereas, the CNTs based ink has gelan gum as an additive to control viscosity, which leaves some room for elastic deformation. The resistive sensor will adopt the mechanical attributes of the substrate the CNTs and GG ink are extruded on.

3.4. Dry chemistry strategy

There are also conductive nanomaterials which are synthesized using dry methods such as sputtering and CVD. The advantage of sputtering is that it can coat conductive material coatings directly on to the target substrate, but the disadvantage here is that the substrate always has to be flat to achieve uniform coating. As the metal oxides and metal films based sensors produced by this way are few, we will be focussing more on carbon based materials. CVD has been used frequently to grow carbon based nanomaterials such as CNTs and graphene on a copper, nickel substrate or silicon wafer. The substrate used to collect the nanomaterials may later be etched away to free the nanomaterials. CVD and a few other methods for carbon based materials have been discussed below.

3.4.1. Pencil trace based electronics. Graphite pencils offer a uniquely simple source of high quality graphene. Fig. 12(a) shows how a bending sensor can be fabricated by simply rubbing a conductive trace on paper.[133] The crumpled graphene layers in the trace can be seen in Fig. 12(d). On application of bending stress, the graphene flakes reorient themselves to establish new percolation networks. Pencils with various concentrations of graphite are available; 9H, 2H, HB, 2B, 6B, 9B, with 9H being the hardest and 9B being the softest. The softest pencils; 9B have the highest content of graphite, hence they are used to fabricate 1D trace based resistive sensors.

3.4.2. 3D foam templating. Coming to CVD methods, instead of a flat nickel substrate, researchers used Ni foam as a scaffold to grow graphene.[149] The Ni was later etched away
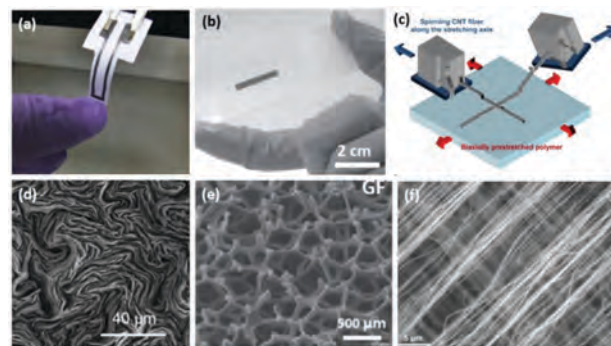

Fig. 12 (a) Pencil graphite trace showing crumpled graphene layers, *Sci. Rep.*, **4**, 3812–3818, Copyright (2014), with permission from Nature.[133] (b) Ni foam templated CVD graphene foam, *Adv. Funct. Mater.*, **25**, 4228–4236, Copyright (2015), with permission from John Wiley and Sons.[147] (c) CNTs fibres from CVD grown vertical CNTs forest, *ACS Nano*, **9**, 5929–5936, Copyright (2015), with permission from American Chemical Society.[148] (d–f) Respective magnifications of the row above.

leaving behind a graphene foam, seen in Fig. 12(e).[147] This graphene foam was fragmentised and turned into an isopropyl alcohol (IPA) based solution. The solution was drop casted into a rectangular shape, which was infiltrated with PDMS upon drying to yield a strain sensor. This unique 3D branched structure transposed onto the graphene from the Ni foam helps to establish a successful percolation network till more than 75% strain. Simple graphene films based sensor usually can't stretch more than 10%.[150] Even with rippled structures achieved using pre-stretching, graphene films can only stretch till about 20%.[113]

3.4.3. Dry-spinning. CNTs films have been grown as vertical dense forests, which can very easily be spun into fibres or transferred onto the target substrate. Due to this spinning ability they can stretch as much as 900% and still maintain a percolation network.[148] The CNTs may be very easily transferred orthogonally to each other on an ecoflex substrate to get biaxial stretchability. The CNTs are obtained as neatly aligned arrays when pulled, with the CNTs in the fibre bonded to each other end to end by van der Waals forces. Due to this the CNTs go through a sliding phase and a disconnecting phase when subjected to strain. The strain range may be increased by introducing pre-strain in the ecoflex substrate before the CNTs transfer.

4. Sensor performance evaluation

This section compares the performance of 0D, 1D, 2D, and hybrid materials as strain and pressure sensors. The comparison is made in terms of sensing range, sensitivity, hysteresis, and durability. The variations are a product of composition of the sensor material and the fabrication methods. The following sections elaborate on this.

4.1. Sensing range

Put simply the range of a sensor falls between the upper and lower limit of its functioning ability. For a strain sensor this would the range between the smallest measurable strain value and the largest measurable strain where the sensor is

still functional. Similarly, for pressure sensors the range falls between the smallest measurable load and the largest load before the sensor becomes completely conducting, or the resistance value becomes unchanging.

The stretchability of a strain sensor depends immensely on the type of NPs used and their dimensions, interaction of conductive NPs with the polymer matrix, construction and fabrication method of the sensor. It is clearly evident from the strain sensor data from previous literature,[78,81,94,122,151–153] that 1D NPs provide the largest strain ranges.[79,82,84,114,123,147,154–156] The largest till date is 960% using CNTs, with a decent gauge factor (GF) of 64.[148] The metal NWs show stretchability till 150% having GFs > 30.[81,94] The large aspect ratios of the particles, 1000–2000, causes a single NW to be in contact with 1000–2000 NWs, as explained in the previous sections. This enables a percolation network to be maintained even when much of the NWs may become disconnected due to sliding or out-of-plane buckling. In contrast low aspect ratio 0D NPs and evaporated films (which also form NPs films) on the other hand have strain ranges $\leq$10%.[76,93,123] Even graphene in a continuous film form has a strain limit <10%,[154] but when it is combined with a 3D scaffold, branched structure, or even a support 1D fibre, its strain range can dramatically increase to almost 700%.[78,147,155] Hence, fabrication method plays a huge role in enhancing sensing range. Finally, the polymer matrix and the conductive fillers should also be compatible with each other in order to not have phase separation after cyclic tests.[78,81,94,114,122,151–153] In case the NPs being used as a film on the polymer substrate, there should be enough bonding between the two to prevent delamination, but also enough pliability to allow buckling for pre-stretching and macro/micro scale patterning. A compromise on the polymer and NPs interaction will reduce the final stretchability. The volume fraction of the NPs will decide the degree of flexibility, stretchability, and self-healing ability of the composite.[79,82,84,123,147,154–156]

In case of pressure sensors, the earlier parameters' influence is reversed. The volume fraction of the NPs needs to be just at the percolation network so as to exhibit a decrease in resistance, due to increase in pressure induced NPs connections.[93,102,114,140,153] As the deformation in a pressure sensor enhances the percolation network reversibly, the focus here lies in balancing the NPs concentration in the composite matrix. Usually the conductive filler composite pressure sensors are used for high pressure ranges, whereas the microfabrication based sensors are used for detecting low pressures.[120,137,151,157]

4.2. Figure of merit

There are many variables governing sensitivity. When it depends on the NPs used dispersed in a polymer matrix then the sensitivity may be tuned to a certain extent by altering concentrations, and the NPs dimensions, to influence resistive mechanisms. But when microfabrication is used to tune sensor features then it is possible to accurately align sensitivity with a sensing range.[69]

The trend which dictates stretchability in strain sensors has an inverse effect on the sensitivity. A large strain range often

relates to low sensitivity and *vice versa*. 0D NPs and evaporated/CVD films tend to form weak percolation networks. Therefore their response in terms of resistance changes is much more drastic than for 1D NPs based percolation networks. A few unique works such as the interlocking Pt coated PDMS micro-pillar array based bilayer pressure/strain sensor have enhanced sensitivity due to their construction. This architecture utilises the 1D micro-pillar's increased surface area, along with the microstructure array coated with Pt, which gives it the enhanced sensitivity from evaporated film sensors.[112] This complex architecture reduced its strain range to only 5%, with a decent sensitivity of 8.3 GF. The work by Xiao *et al.* shows polystyrene nanofibers with vertical growth of ZnO NWs from the surface. It has a more efficient interlocking system, and the resultant sensitivity is 116 GF, with a maximum strain range of 50%.[75] A flat 2D and comparatively simpler designed guided micro-crack based sensor on the other hand has a strain range of 10%, but an extraordinary sensitivity of 2×10^6 GF.[93]

The interlocking Pt coated PDMS micro-pillar array sensor has a better performance as a pressure sensor, as the microstructure is properly taken advantage of here. As pressure sensors have much simpler way of transduction compared to strain sensors, their sensitivities can simply be predicted by observing the kind of NPs used, and the method of fabrication of the sensor. From literature data,[79,84,123,147,154,155] it can be deduced that microfabrication based sensors have the highest sensitivities,[78,93,94,102,114,120,137,140,151,153,157] followed by 0D/2D and 1D.[81,82,94,122,151,152,156] Often surface asperities, and obvious roughness is used to concentrate the pressure signal.[112,120] But sometimes a simpler designed guided micro-crack based sensor can achieve an extraordinarily high sensitivity of 136018.16 kPa^{-1} with a maximum pressure of 9.5 kPa.[93,112]

4.3. Hysteresis and durability

Hysteresis is particularly important for resistive e-skin sensors, especially sensors used to measure joint movements and physiological signals such as respiration and heart beats. These sensors would be enduring constant dynamic load. If hysteresis is not kept under check under such conditions, it may lead to progressively worsening degradation of the percolation network resulting in poor performance of the sensor over long durations of dynamic stimuli.[33] Hysteresis is caused in different ways depending on the construction of the sensors. In composites where the NPs are dispersed in the polymer matrix, the majority of the hysteresis is caused by the viscoelastic behaviour of the polymer. This is usually the lag time the sensor exhibits to return to a baseline reading, which is caused by the "sluggishness" in the elastic behaviour of the polymer matrix. The interaction between the type of NPs fillers and the polymer matrix can also contribute to hysteresis. If the bonding between rigid NPs such as NWs, and the elastomer matrix needs to be weak enough, so that on application of strain the displaced nanomaterials will be slide back to their original positions. On having a strong interfacial interaction, large strains may result in fracture and buckling of the NPs due to friction between the polymer and NPs on release of the stress/strain.

Softer carbon based NPs require that the interfacial binding is strong with the polymer matrix. A weak binding allows the NPs to slide under strain, but they are not able to return to their original positions completely on release of the strain. This will cause progressive phase separation of the NPs from the polymer matrix resulting in hysteresis behaviour. This is particularly common in CNTs based composites. Therefore pairing the right polymer matrix with the right NPs will ensure minimum hysteresis in the sensor. In essence, by preventing hysteresis, a sensor can be made to last longer without degradation and hence become very durable.

5. Applications

5.1. Robotic controlling & sport performance assessment

Human–machine interfaces and robotic remote controlling are greatly beneficial in surgery or highly risky work that required the replacement of robotics.[134] In these applications, the sensors are built up as a skin-like device to attach on human body or machine system.[90,158] Generally, for robotics and sport performance assessment, the sensors are typically mounted on body joint like fingers,[159] elbows, knees, or ankles which are normally bended or stretched at large degree of deformations, thus the sensors are required to have high stretchability ($\geq 50\%$) in order to able to maintain the conductivity as stretching.[155,160–162]

The robotic controlling by flexible and stretchable sensors is demonstrated in Fig. 13(a and b), and the stretchable strain sensors were based on the hybrid of polyaniline and gold nanowires for a smart glove.[81] The sensor based-smart glove is used to control the movement of a robot through wireless signals (Fig. 13(a)). The robot is at relaxed state (a_1) and works as an arm that can clamp (a_2), lift up (a_3), put down (a_4) and release (a_5) an object based on different postures of human fingers as wearing the sensor. Fig. 13(b) reveals the remote control on the robot movement by a strain sensor based on graphene platelet material.[92] As can be seen in this figure, b_1 and b_4 demonstrate the robot at the relaxed state. As the strain sensor is stretched or bended, the robot is started working (b_2 and b_5) and moving to the controller (b_3 and b_6).
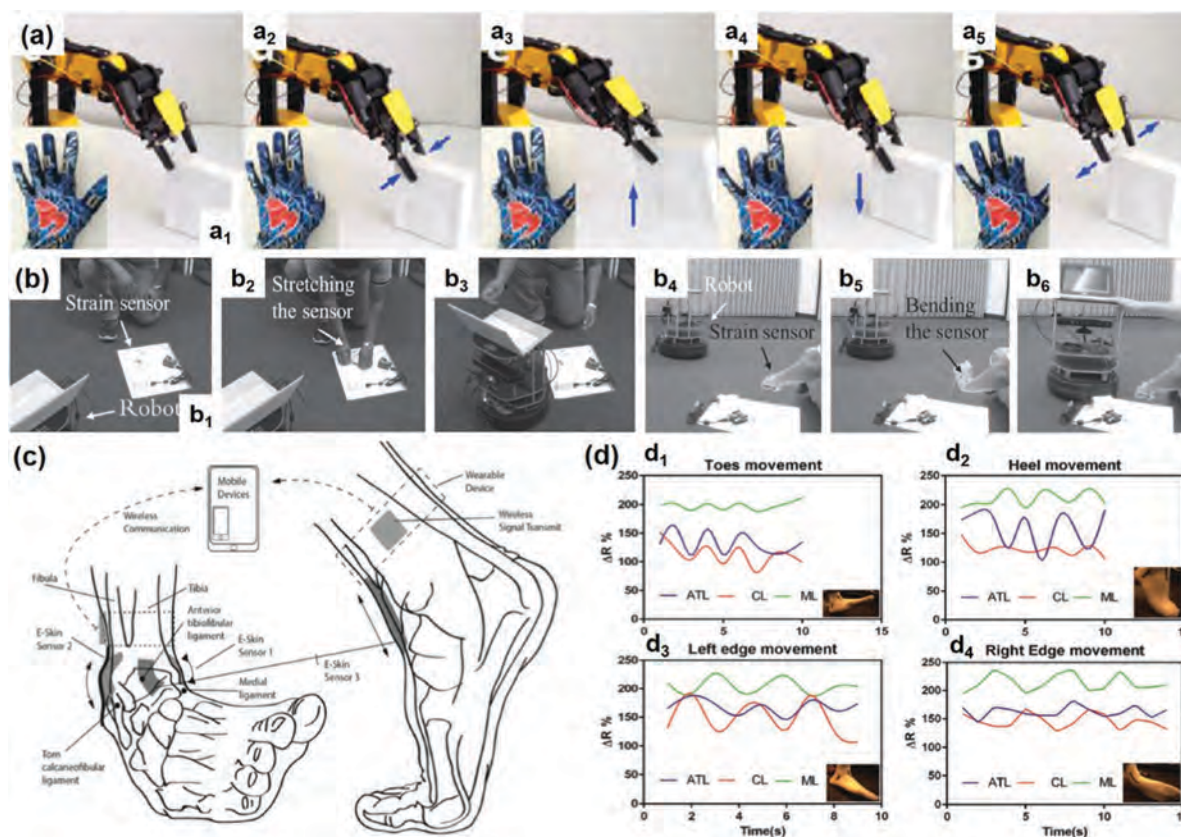

Fig. 13 Piezoresistive sensors for posture monitoring and sports performance assessment. (a) Smart gloves for relaxed state (a_1), object clamping (a_2), object up-lifting (a_3), object putting-down (a_4), object releasing (a_5), *ACS Appl. Mater. Interfaces*, **7**, 19700–19708, Copyright (2015), with permission from American Chemical Society.[81] (b) Tensile strain (b_1, b_2, b_3) and wrist bending (b_4, b_5, b_6) for robotic controlling. (b_1, b_4) Relaxation state, (b_2, b_5) strain state as the robot started moving, and (b_3, b_6) the robot moving to the user, *Adv. Funct. Mater.*, **26**, 7614–7625, Copyright (2016), with permission from John Wiley and Sons.[92] (c) Schematic illusion of CuNW/GrMF/CuNW sensors attached on different positions of the human ankle corresponding to the anterior tibiofibular ligament (ATL), calcaneofibular ligament (CL), and medial ligament (ML). (d) Time-dependent resistance change of the strain sensor on (d_1) toes and (d_2) heel up-down movement, and side-to-side hinge movement on the left (d_3) and right foot edge, *Nanoscale*, **8**, 16596–16605. Copyright (2016) with permission from The Royal Society of Chemistry.[94]

On the other hand, as wearing the sensor on various positions of human body, the wearable sensors also enable us to monitor muscle movements continuously during daily activities. This can be applied to assess sport performance and improving human fitness, especially for athletes.[152,153] Demonstrating in Fig. 13(c) is the CuNW/GrMF/CuNW sensors attached on the human ankle to monitor the movement of different positions such as the anterior tibiofibular ligament (ATL), calcaneofibular ligament (CL), and medial ligament (ML).[94] The sensors are also connected to the wireless device to detect the activities in real time. Fig. 1(d) illustrates the time-dependent resistance change of the sensors corresponding to the toes (d_1), heel (d_2), left edge (d_3) and right edge (d_4) movement.

5.2. Cardiac impulses, respiration rate, pulses and blood pressure sensing

Detecting small but critical signals like cardiac impulse, respiration rate, pulse and blood pressure is an important part of wearable medical healthcare system. Wearing the sensors for long-term sensing of these signals enable us to diagnose several diseases at early stages. The sensors for these applications are required to be highly sensitive at low strain regime ($\leq 5.0\%$ strain) since the degree of deformations are relatively small in comparison with that of body joints as discuss above.

You *et al.* developed a gold nanoparticle based sensor enables to detect the respiration rate and real-time monitoring heart beats wirelessly through a portable smart device.[163] Fig. 14(a) indicates

the position where attached the sensor on and Fig. 14(b) shows the diagram of the sensor connecting to a portable device through the wireless device. In this work, the e-skin apexcardiogram (ACG) is mainly focused for diagnosing heart disease instead of the electrocardiogram (ECG). The advantages of the ACG is that it is helpful in sensing various diseases related to the human heart such as atrial fibrillation, valve diseases, anemia, and myocardial infarction which are difficult to detect by using the ECG technique.

For pulse monitoring, we introduced an ionic liquid based-strain sensor attached on the wrist as a wearable band which is able to sense the wrist pulse (Fig. 14(c)).[72] The sensors are fabricated by 3D printing and demonstrate a capability to sense from a very small strain ($\sim 0.1\%$ strain) to an extremely large strain ($\sim 500\%$ strain). The sensitivity and the stretchability of this liquid-based sensor are basically tunable by the diameter of the sensors. Furthermore, Lou *et al.* fabricated a sensor comprising a flexible resistive strain sensor and a epidermal ECG sensor which is used for cuffless blood pressure (Fig. 14(d)).[164] Digital images of the resistive sensor and the sensor system including the resistive sensor connected with the ECG sensor are shown in the top row of Fig. 14(d). The lower row reveals the typical ECG waveform and the measure wrist pulses by the sensor system. The blood pressure including the systolic phase and the diastolic phase can be calculated from these pulse signals as well.

5.3. Voice sensing and facial emotion detection

Voice recognition and facial emotion detection are vital for some specific applications such as security, or entertaining system.[165,166] Additionally, it is also useful for patients who have problems with muscle control after stroke. These applications do not require very large stretchability from the sensor, since the deformations being measured are moderate. However, transparent property is preferable in this case since the sensors are mounted on the visible parts like face or neck.

Park *et al.* fabricated the platinum based-sensor based on crack mechanism for voice sensing.[167] As can be seen in Fig. 15(a), the crack sensor is attached on human neck and the frequency spectrum of voice tone of C, D, E, F, A, B, C with high GF (16k, top) and low GF (2k, bottom) sensors is revealed in Fig. 15(b). Towards this direction, an innovative and facile way to develop ultra-strain bearing and sensitive resistive sensors was developed recently by Wang *et al.*, Fig. 15(e and g).[168] By carbonizing silk fabric, the researchers were able to take advantage of the natural inter-woven structure of the silk fibres in the fabric, which resulted in a stretchability of $\sim 500\%$. The sensor can accurately detect voice intonations when speaking different words, Fig. 15(f). It is also able to replicate to a large extent the sound wave profile of audio being played through an earphone speaker, Fig. 15(h).

A stretchable transparent sensor based on a hybrid of PU–PEDOT:PSS and CNT is introduced by Roh *et al.* for facial emotion detection.[156] For this application, since the sensor is attached on the human face, therefore the achieved transparency of about 62% is very conducive for users to be more comfortable with wearing the sensor during their daily activities.
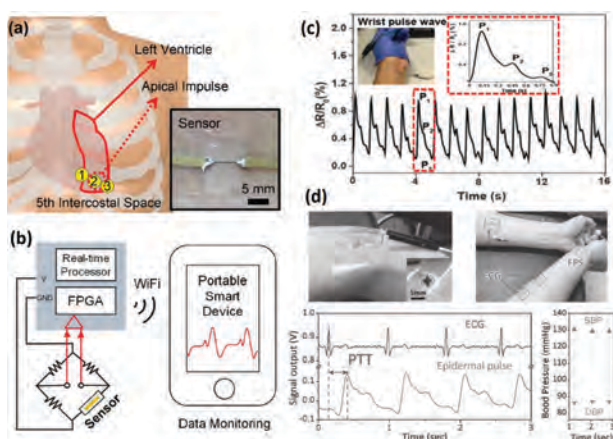

Fig. 14 Piezoresistive sensors for sensing cardiac impulses, wrist pulses and blood pressure. (a) Schematic illusion indicating the attached locations of the ACG sensor (inset: a digital image of the sensor). (b) The block diagram of the ACG sensor and the wireless connection to a portable electronic device (bottom), *Adv. Mater.*, 6359–6364. Copyright (2016), with permission from John Wiley and Sons.[163] (c) Time-dependent relative resistance change of the ionic based-strain sensor for wrist pulse monitoring (inset: a waveform of a typical wrist pulse), *Mater. Horiz.*, **3**, 208–213. Copyright 2016, reproduced from ref. 72 with permission from the Royal Society of Chemistry.[72] (d) Top piezoresistive sensors for cuffless blood pressure; top left, (inset: the active region of the sensor), the sensor connected to electrocardiogram (ECG) sensors; top right, time-dependent electrical signals of the system of the sensor and the ECG demonstrating the transit time (PTT); bottom left, systolic blood pressure (SBP) and diastolic blood pressure (DBP) that calculated from the ECG and the epidermal pulse signals; bottom right, *Adv. Funct. Mater.*, **26**, 1178–1187, Copyright (2016), with permission from John Wiley and Sons.[164]

Fig. 15(c) illustrates different positions including forehead, under the eye, near the mouth and neck that the sensor was attached for sensing emotional expressions. Fig. 15(d) shows the relative resistance change of the transparent sensor attached on the forehead (d_1, d_2) and nearby the mouth (d_3, d_4) during laughing and crying, respectively.

5.4. Invisibles-future of wearables

Sensors have been made thin and conformable enough that they can be adhered on human skin like an imperceptible bandage.[169] Now the next exciting challenge for the new generation of sensors is to make them invisible, Fig. 16(a). Combining these invisible sensors with their own power source as shown in Fig. 16(b).[170,171] The strain sensor is constructed of a 1D AgNWs, PEDOT:PSS,
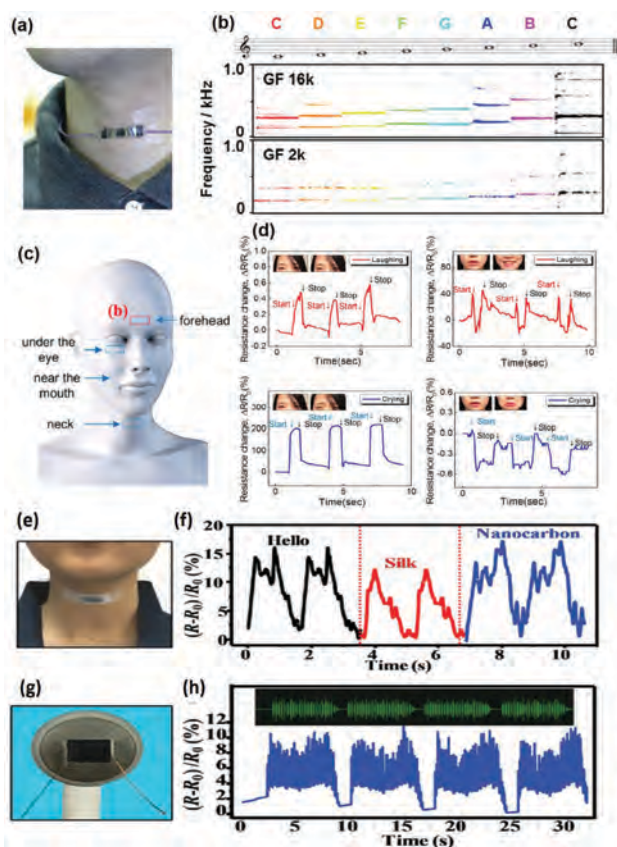

Fig. 15 Resistive sensors for voice sensing and facial emotion detection. (a) Crack sensor attached on a human neck for voice sensing. (b) The frequency spectrum of voice tone of C, D, E, F, A, B, C with high GF (16k, top) and low GF (2k, bottom) sensors, *Adv. Mater.*, **28**, 8130–8137, Copyright (2016), with permission from John Wiley and Sons.[167] (c) Schematic illusion showing different positions on faces and neck that the stretchable and transparent sensors attached on. (d) The time-dependent relative resistance change of the sensors as attached on the forehead and nearby the mouth, *ACS Nano*, **9**, 6252–6261, Copyright 2015, with permission from, American Chemical Society.[156] (e) Photograph of the sensor attached on throat, (f) electric signals as speaking "Hello," "Silk," and "Nanocarbon". (g) Photograph of the sensor attached on an earphone. (h) Electric signals of the sensor corresponding to a warble audio, inset is the sound wave profile, *Adv. Mater.*, 2016, **28**, 6640–6648, with permission from John Wiley and Sons.[168]

and polyurethane (PU) composite, using spin coating. The same composite is used as electrodes for fabrication of a triboelectric energy generator, and this energy is stored in a PVA/H_3PO_4 based supercapacitor. The whole sensor is 75.3% transparent. This self-powered strain sensor is used to measure various movements of the throat. Fig. 16(c) demonstrates a 2D graphene based invisible biaxial strain sensor, which was fabricated *via* CVD growth and subsequent PDMS stamping technique.[172] The resulting sensor has a 75–80% transmittance.

Finally, we have a micro-crack based 0D sputter coated ITO film which can be used as a pressure and strain sensor, Fig. 16(d).[76] This sensor has the highest transmittance of 89% till now. Due to the contradicting aims of high transparency along with stretchability, the strain limit has been limited to under 10% for these sensors. This is largely due to the sparse percolation network required to maintain transparency in the conductive films. These films on being stretched are expected to lose lot more inter-particle connections, as compared to a non-transparent standard stretchable conductor. Recently, Ho *et al.* reported transparent strains sensors towards "invisible" wearable sensors based on a dual percolating network of AgNWs and AuNWs, Fig. 16(e and f).[173] The combination of two different materials with different electrical and mechanical properties leads to the sensors with high GF ($\sim$236) even at low strain regime ($<$5.0%) and high stretchability ($\sim$70%) and the optical transparent ranging from 58.7% to 66.7% by optimizing the dual percolation network. In addition, these sensors are able to work at only 0.1 V and are fabricated by a simple, room-temperature and cost-effective solution process. Finally, their sensing performance is demonstrated by detecting facial emotions, respiration and apexcardiogram.

Moreover, another work demonstrated that a good strain range of 30% with a decent transmittance of 79% was established for a transparent supercapacitor.[174] Just the electrode of the device can be easily used as a transparent strain sensor with a significantly larger stretchability than the previously discussed cases. The large stretchability was established due to the extraordinary soft hair like morphology, afforded due to the high aspect ratio $\sim$2000, and extremely small diameter of 2 nm of the AuNWs. This allowed for the NWs coating on the elastomer to behave almost like a coating made of polymer chains. It should also be noted that, as a standard non-transparent coating, the sensor can stretch till 350%.[86] These sensors are highly suitable for applications requiring transparency and high sensitivity, such as detecting facial expressions, as shown in Fig. 15(c and d).

5.5. Ionic liquid ultra-durable wearables

Ionic liquids (ILs) offer another solution towards wearables which can also potentially be used to make invisible wearables. As they are essentially transparent or gently tinted liquids, the transparency of the final device is ultimately decided by the encapsulating elastomeric framework of the sensor device. Moreover the Young's modulus of ILs being at least five orders of magnitude lower than that of elastomers, dictates that the final strain measuring function of a device will be limited by elastic framework itself.[175] Hence, extraordinary strain ranges
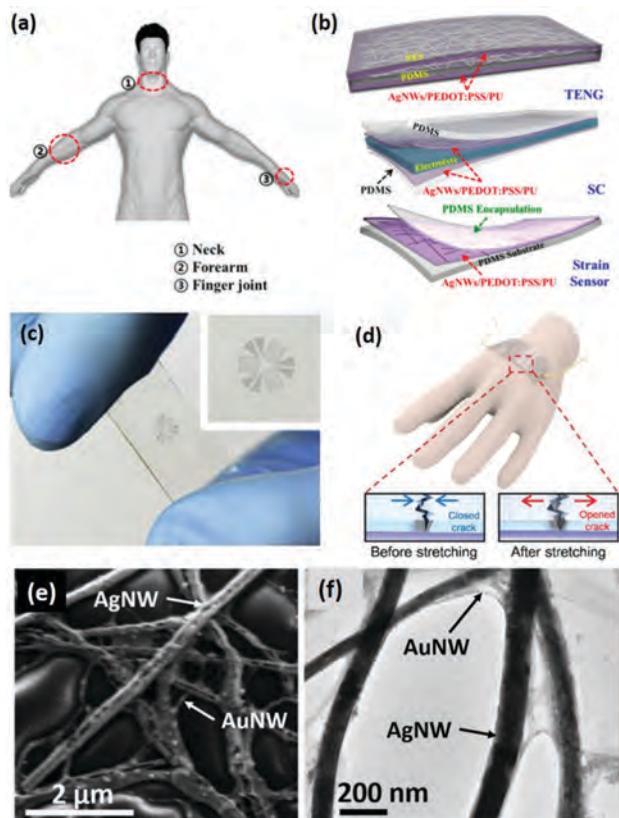
Fig. 16 (a and b) Self-powered AgNWs−PEDOT−PSS−PU strain sensor, *ACS Nano*, **9**, 8801−8810, Copyright (2015), with permission from American Chemical Society.[170] (c) Transparent graphene strain sensor, *Carbon*, **51**, 236−242, Copyright (2013), with permission from Elsevier.[172] (d) Transparent ITO film cracking based strain sensor, *J. Mater. Chem. C*, **4**, 9947−9953, Copyright (2016), reproduced from ref. 76 with permission from the Royal Society of Chemistry.[76] (e) FESEM of AgNWs/AuNWs percolation network on PDMS elastomer. (f) TEM showing ultra-flexible AuNWs bridging the gap between the rigid AgNWs, *Adv. Funct. Mater.*, 2017, 1700845−1700854, Copyright (2017), with permission from John Wiley and Sons.[173]

up to 600% may be achieved.[72,175] The ability of ILs to conform to all volume changes of the channel reservoirs and being "volume invariant" makes them extremely durable. The only part of the device accumulating stress and fatigue over time is the encapsulating elastomer itself. If the channel sealing is robust enough, the sensor may last as long as 6 months with no degradation, in open air or even under water.

ILs based sensors have one crucial drawback. They often tend to suffer from very low sensitivities, GF < 5. This may be improved slightly by the additives like PANI NPs and Au NWs, by providing additional bridges for electron flow.[72] Most of the ILs based sensors use soft silicone rubber based scaffolding and frameworks. The response time is also observed to be quite large due to the lag time generated during the post strain recovery of the elastomeric support structure, as opposed to non ILs based sensors.[46,142] Increasing the conductivity of the ILs composite sensing materials, and integrating it with an elastomer with quick recovery based viscoelastic properties will be one of the future challenges to be tackled.

6. Summary and future perspectives

Resistance sensing is one of the popular transduction based mechanisms, namely piezoelectricity, triboelectricity, and capacitance, which are used to measure various physical stimuli. The other transduction mechanisms may have their strengths such as extreme pressure sensitivity, and proximity measurements for capacitive sensors, sensing and also simultaneous energy generation with piezoelectric, and triboelectric sensors. Resistive sensors attract strong recent attention because of their ease in construction and measurement of readings with very simple equipment. Resistive sensor devices were originally a thin metal strip with numerous closely spaced bends used to measure minute changes in dimensions of architectural support, and plumbing structures. Today they have been completely reimagined and have been elevated to the status of E-skin devices. This has been possible due to the wealth of nanomaterials of various dimensions and conductivities being designed and synthesized over the years.

Manufacture of resistive sensor devices from these materials requires fundamental understanding of percolation mechanisms and the various device fabrication methods. Especially, the working mechanism of resistive sensors, and the kinds of percolation networks formed by 0D, 1D, and 2D materials, conducting polymers, inorganic oxides and hybrid materials. Study of the dynamic changes occurring in percolation networks when under stress/strain contribute to the deep understanding of crack and tear propagation in the sensor materials. This knowledge is crucial when designing conductive composite materials with a particular conductive nanoparticle filler. Self-healing sensors are a direct solution to problems such as fatigue and tearing, which results in enhanced endurance and consistent measurements. In addition, enhancement to the stretchability and sensitivity of the sensors can be achieved by means of macroscale and microscale patterning and substrate modification.

Furthermore, using the numerous wet and dry ink formation and corresponding ink delivery methods on elastomers, resistive e-skin sensors of various dimensions can be fabricated. These include 1D trace, 2D coatings, and 3D sponge-form resistive devices. The performance of these sensors and their limitations are based on the kind of nanomaterials used and the fabrication methods. Finally, the resistive e-skin sensors are used in key applications, which include robotic controlling, ergonomics, sports performance, and cardiac monitoring.

Currently, research on invisible e-skins is already underway, as shown in Fig. 16, with good stretchability reaching almost 80%. The only minor hurdle is to transfer this sensor onto an extremely thin skin like transparent elastomer membrane. This might prove a little tricky. The other drawback is the slow response time of resistive e-skin sensors, as compared to other transduction methods. This is especially prevalent in ILs based sensors. These few but important challenges still remain at this stage. Even so, we may still imagine that in the near future simple, thin resistive materials may become second-skin like. They will ultimately be a part of a self-powered, imperceptible,

and invisible device which is seamlessly integrated with the human body. Such a device will be constantly interfacing with us and our environment, and will add another dimension to our perception of ourselves and our surrounding environments as a whole.

Acknowledgements

References

1 B. Deng, P. Hsu, G. Chen, B. N. Chandrashekar, L. Liao, Z. Ayitimuda, J. Wu, Y. Guo, L. Lin, Y. Zhou, M. Aisijiang, Q. Xie, Y. Cui, Z. Liu and H. Peng, *Nano Lett.*, 2015, **15**, 4206–4213.

2 S. Bae, H. Kim, Y. Lee, X. Xu, J.-S. Park, Y. Zheng, J. Balakrishnan, T. Lei, H. R. Kim, Y. Il Song, Y.-J. Kim, K. S. Kim, B. Ozyilmaz, J.-H. Ahn, B. H. Hong and S. Iijima, *Nat. Nanotechnol.*, 2010, **5**, 574–578.

3 D. Angmo, T. T. Larsen-Olsen, M. Jørgensen, R. R. Søndergaard and F. C. Krebs, *Adv. Energy Mater.*, 2013, **3**, 172–175.

4 F. C. Krebs, J. Fyenbo and M. Jørgensen, *J. Mater. Chem.*, 2010, **20**, 8994.

5 C. Feng, K. Liu, J. S. Wu, L. Liu, J. S. Cheng, Y. Zhang, Y. Sun, Q. Li, S. Fan and K. Jiang, *Adv. Funct. Mater.*, 2010, **20**, 885–891.

6 M. Park, J. Im, M. Shin, Y. Min, J. Park, H. Cho, S. Park, M.-B. Shim, S. Jeon, D.-Y. Chung, J. Bae, J. Park, U. Jeong and K. Kim, *Nat. Nanotechnol.*, 2012, **7**, 803–809.

7 Q. Li and X. M. Tao, *Proc. R. Soc. London, Ser. A*, 2014, **470**, 20140472.

8 L. Persano, C. Dagdeviren, Y. Su, Y. Zhang, S. Girardo, D. Pisignano, Y. Huang and J. A. Rogers, *Nat. Commun.*, 2013, **4**, 1633.

9 H. Qi, B. Schulz, T. Vad, J. Liu, E. Mäder, G. Seide and T. Gries, *ACS Appl. Mater. Interfaces*, 2015, **7**, 22404–22412.

10 C. Mattmann, F. Clemens and G. Tröster, *Sensors*, 2008, **8**, 3719–3732.

11 S. J. Tan, M. J. Campolongo, D. Luo and W. Cheng, *Nat. Nanotechnol.*, 2011, **6**, 268–276.

12 Y. C. Lu and K. S. Chou, *Nanotechnology*, 2010, **21**, 215707.

13 J. Lee, I. Lee, T.-S. Kim and J.-Y. Lee, *Small*, 2013, 1–8.

14 S. Luo and T. Liu, *Adv. Mater.*, 2013, **25**, 5650–5657.

15 L. Hu, H. S. Kim, J. Lee, P. Peumans and Y. Cui, *ACS Nano*, 2010, **4**, 2955–2963.

16 V. Scardaci, R. Coull, P. E. Lyons, D. Rickard and J. N. Coleman, *Small*, 2011, **7**, 2621–2628.

17 J.-A. Jeong and H.-K. Kim, *Appl. Phys. Lett.*, 2014, **104**, 71906.

18 S.-B. Kang, Y.-J. Noh, S.-I. Na and H.-K. Kim, *Sol. Energy Mater. Sol. Cells*, 2014, **122**, 152–157.

19 J.-A. Jeong, Y.-J. Jeon, S.-S. Kim, B. Kyoung Kim, K.-B. Chung and H.-K. Kim, *Sol. Energy Mater. Sol. Cells*, 2014, **122**, 241–250.

20 J.-H. Lee, H.-S. Shin, Y.-J. Noh, S.-I. Na and H.-K. Kim, *Sol. Energy Mater. Sol. Cells*, 2013, **114**, 15–23.

21 L. Polavarapu, A. La Porta, S. M. Novikov, M. Coronado-Puchau and L. M. Liz-Marzán, *Small*, 2014, **10**, 3065–3071.

22 H. Warren, R. D. Gately, H. N. Moffat and M. in het Panhuis, *RSC Adv.*, 2013, **3**, 21936.

23 Z. Li, H. Liu, C. Ouyang, W. Hong Wee, X. Cui, T. Jian Lu, B. Pingguan-Murphy, F. Li and F. Xu, *Adv. Funct. Mater.*, 2016, **26**, 165–180.

24 N. Dossi, F. Terzi, E. Piccin, R. Toniolo and G. Bontempelli, *Electroanalysis*, 2016, **28**, 250–264.

25 S. A. Odom, S. Chayanupatkul, B. J. Blaiszik, O. Zhao, A. C. Jackson, P. V. Braun, N. R. Sottos, S. R. White and J. S. Moore, *Adv. Mater.*, 2012, **24**, 2578–2581.

26 W. Shen, X. Zhang, Q. Huang, Q. Xu and W. Song, *Nanoscale*, 2014, **6**, 1622–1628.

27 A. M. J. van den Berg, A. W. M. de Laat, P. J. Smith, J. Perelaer and U. S. Schubert, *J. Mater. Chem.*, 2007, **17**, 677–683.

28 J. Lessing, A. C. Glavan, S. B. Walker, C. Keplinger, J. A. Lewis and G. M. Whitesides, *Adv. Mater.*, 2014, **26**, 4677–4682.

29 B. Dan, G. C. Irvin and M. Pasquali, *ACS Nano*, 2009, **3**, 835–843.

30 M. Hu, J. Gao, Y. Dong, K. Li, G. Shan, S. Yang and R. K.-Y. Li, *Langmuir*, 2012, **28**, 7101–7106.

31 A. B. V. Kiran Kumar, C. Wan Bae, L. Piao and S.-H. Kim, *Mater. Res. Bull.*, 2013, **48**, 2944–2949.

32 Y. Aleeva and B. Pignataro, *J. Mater. Chem. C*, 2014, **2**, 6436.

33 M. Amjadi, K. U. Kyung, I. Park and M. Sitti, *Adv. Funct. Mater.*, 2016, **26**, 1678–1698.

34 M. Amjadi, A. Pichitpajongkit, S. Lee, S. Ryu and I. Park, *ACS Nano*, 2014, **8**, 5154–5163.

35 E.-S. Hwang, J. Seo and Y.-J. Kim, *J. Microelectromech. Syst.*, 2007, **16**, 556–563.

36 J. Park, M. Kim, Y. Lee, H. S. Lee and H. Ko, *Sci. Adv.*, 2015, **1**, e1500661.

37 J. Zhong, Q. Zhong, Q. Hu, N. Wu, W. Li, B. Wang, B. Hu and J. Zhou, *Adv. Funct. Mater.*, 2015, **25**, 1798–1803.

38 G. Ren, F. Cai, B. Li, J. Zheng and C. Xu, *Macromol. Mater. Eng.*, 2013, **298**, 541–546.

39 M. Ha, S. Lim, J. Park, D. S. Um, Y. Lee and H. Ko, *Adv. Funct. Mater.*, 2015, **25**, 2841–2849.

40 J.-W. Zhao, Y.-F. Zhang, Y.-H. Li, C. Su, X.-M. Song, H. Yan and R.-Z. Wang, *Sci. Rep.*, 2016, **5**, 17692.

41 S. Zhao, S. Fathololoumi, K. H. Bevan, D. P. Liu, M. G. Kibria, Q. Li, G. T. Wang, H. Guo and Z. Mi, *Nano Lett.*, 2012, **12**, 2877–2882.

42 S. K. Ghosh and D. Mandal, *Appl. Phys. Lett.*, 2016, **109**, 103701.

43 G. Zhu, W. Q. Yang, T. Zhang, Q. Jing, J. Chen, Y. S. Zhou, P. Bai and Z. L. Wang, *Nano Lett.*, 2014, **14**, 3208–3213.

44 S. Park, H. Kim, M. Vosgueritchian, S. Cheon, H. Kim, J. H. Koo, T. R. Kim, S. Lee, G. Schwartz, H. Chang and Z. Bao, *Adv. Mater.*, 2014, **26**, 7324–7332.

45 D. J. Cohen, D. Mitra, K. Peterson and M. M. Maharbiz, *Nano Lett.*, 2012, **12**, 1821–1825.

46 C. M. Boutry, A. Nguyen, Q. O. Lawal, A. Chortos, S. Rondeau-Gagné and Z. Bao, *Adv. Mater.*, 2015, **27**, 6954–6961.

47 Z.-M. Dang, Y.-H. Lin and C.-W. Nan, *Adv. Mater.*, 2003, **15**, 1625–1629.

48 M. Panda, V. Srinivas and A. K. Thakur, *Appl. Phys. Lett.*, 2008, **92**, 1–4.

49 W. Bauhofer and J. Z. Kovacs, *Compos. Sci. Technol.*, 2009, **69**, 1486–1498.

50 N. Hu, Y. Karube, M. Arai, T. Watanabe, C. Yan, Y. Li, Y. Liu and H. Fukunaga, *Carbon*, 2010, **48**, 680–687.

51 F. He, S. Lau, H. L. Chan and J. Fan, *Adv. Mater.*, 2009, **21**, 710–715.

52 M. Hempel, D. Nezich, J. Kong and M. Hofmann, *Nano Lett.*, 2012, **12**, 5714–5718.

53 M. Park, J. Park and U. Jeong, *Nano Today*, 2014, **9**, 244–260.

54 Y. Kim, J. Zhu, B. Yeom, M. Di Prima, X. Su, J.-G. Kim, S. J. Yoo, C. Uher and N. A. Kotov, *Nature*, 2013, **500**, 59–63.

55 W. P. Shih, L. C. Tsao, C. W. Lee, M. Y. Cheng, C. Chang, Y. J. Yang and K. C. Fan, *Sensors*, 2010, **10**, 3597–3610.

56 J. Li and J. K. Kim, *Compos. Sci. Technol.*, 2007, **67**, 2114–2120.

57 A. Russo, B. Y. Ahn, J. J. Adams, E. B. Duoss, J. T. Bernhard and J. A. Lewis, *Adv. Mater.*, 2011, **23**, 3426–3430.

58 C. Yang, C. P. Wong and M. M. F. Yuen, *J. Mater. Chem. C*, 2013, **1**, 4052.

59 J. Li, P. C. Ma, W. S. Chow, C. K. To, B. Z. Tang and J. K. Kim, *Adv. Funct. Mater.*, 2007, **17**, 3207–3215.

60 A. G. MacDiarmid, *Synth. Met.*, 2001, **125**, 11–22.

61 M. Hasegawa and M. Iyoda, *Chem. Soc. Rev.*, 2010, **39**, 2420–2427.

62 C. K. Chiang, C. R. Fincher, Y. W. Park, A. J. Heeger, H. Shirakawa, E. J. Louis, S. C. Gau and A. G. MacDiarmid, *Phys. Rev. Lett.*, 1977, **39**, 1098–1101.

63 C. K. Chiang, M. A. Druy, S. C. Gau, A. J. Heeger, E. J. Louis, A. G. MacDiarmid, Y. W. Park and H. Shirakawa, *J. Am. Chem. Soc.*, 1978, **100**, 1013–1015.

64 P. J. Nigrey, D. MacInnes, D. P. Nairns and A. G. MacDiarmid, *J. Electrochem. Soc.*, 1981, **128**, 1651.

65 P. J. Nigrey, A. G. MacDiarmid and A. J. Heeger, *J. Chem. Soc., Chem. Commun.*, 1979, 594.

66 S. Savagatrup, A. D. Printz, T. F. O'Connor, A. V. Zaretski and D. J. Lipomi, *Chem. Mater.*, 2014, **26**, 3028–3041.

67 L. Pan, A. Chortos, G. Yu, Y. Wang, S. Isaacson, R. Allen, Y. Shi, R. Dauskardt and Z. Bao, *Nat. Commun.*, 2014, **5**, 1–8.

68 C. Hou, T. Huang, H. Wang, H. Yu, Q. Zhang and Y. Li, *Sci. Rep.*, 2013, **3**, 3138.

69 H.-H. Chou, A. Nguyen, A. Chortos, J. W. F. To, C. Lu, J. Mei, T. Kurosawa, W.-G. Bae, J. B.-H. Tok and Z. Bao, *Nat. Commun.*, 2015, **6**, 8011.

70 X. Han, X. Chen, X. Tang, Y.-L. Chen, J.-H. Liu and Q.-D. Shen, *Adv. Funct. Mater.*, 2016, **26**, 3640–3648.

71 J. Song, S. A. Kulinich, J. Li, Y. Liu and H. Zeng, *Angew. Chem., Int. Ed.*, 2015, **54**, 462–466.

72 Y. Wang, S. Gong, S. J. Wang, G. P. Simon and W. Cheng, *Mater. Horiz.*, 2016, **3**, 208–213.

73 K.-Y. Chun, Y. Oh, J. Rho, J.-H. Ahn, Y.-J. Kim, H. R. Choi and S. Baik, *Nat. Nanotechnol.*, 2010, **5**, 853–857.

74 R. M. Pasquarelli, D. S. Ginley and R. O'Hayre, *Chem. Soc. Rev.*, 2011, **40**, 5406–5441.

75 X. Xiao, L. Yuan, J. Zhong, T. Ding, Y. Liu, Z. Cai, Y. Rong, H. Han, J. Zhou and Z. L. Wang, *Adv. Mater.*, 2011, **23**, 5440–5444.

76 T. Lee, Y. W. Choi, G. Lee, P. V. Pikhitsa, D. Kang, S. M. Kim and M. Choi, *J. Mater. Chem. C*, 2016, **4**, 9947–9953.

77 S. Luo and T. Liu, *Adv. Mater.*, 2013, **25**, 5650–5657.

78 C. Yan, J. Wang, W. Kang, M. Cui, X. Wang, C. Y. Foo, K. J. Chee and P. S. Lee, *Adv. Mater.*, 2014, **26**, 2022–2027.

79 K. Takei, Z. Yu, M. Zheng, H. Ota, T. Takahashi and A. Javey, *Proc. Natl. Acad. Sci. U. S. A.*, 2014, **111**, 1703–1707.

80 J. Shi, X. Li, H. Cheng, Z. Liu, L. Zhao, T. Yang, Z. Dai, Z. Cheng, E. Shi, L. Yang, Z. Zhang, A. Cao, H. Zhu and Y. Fang, *Adv. Funct. Mater.*, 2016, **26**, 2078–2084.

81 S. Gong, D. T. H. Lai, Y. Wang, L. W. Yap, K. J. Si, Q. Shi, N. N. Jason, T. Sridhar, H. Uddin and W. Cheng, *ACS Appl. Mater. Interfaces*, 2015, **7**, 19700–19708.

82 T. Yamada, Y. Hayamizu, Y. Yamamoto, Y. Yomogida, A. Izadi-Najafabadi, D. N. Futaba and K. Hata, *Nat. Nanotechnol.*, 2011, **6**, 296–301.

83 S. De, P. J. King, P. E. Lyons, U. Khan and J. N. Coleman, *ACS Nano*, 2010, **4**, 7064–7072.

84 J. Lee, S. Kim, J. Lee, D. Yang, B. C. Park, S. Ryu and I. Park, *Nanoscale*, 2014, **6**, 11932–11939.

85 H. Tian, Y. Shu, Y.-L. Cui, W.-T. Mi, Y. Yang, D. Xie and T.-L. Ren, *Nanoscale*, 2014, **6**, 699–705.

86 S. Gong, D. T. H. Lai, B. Su, K. J. Si, Z. Ma, L. W. Yap, P. Guo and W. Cheng, *Adv. Electron. Mater.*, 2015, **1**, 1400063.

87 I. M. Graz, D. P. J. Cotton and S. P. Lacour, *Appl. Phys. Lett.*, 2009, **94**, 71902.

88 S. P. Lacour, D. Chan, S. Wagner, T. Li and Z. Suo, *Appl. Phys. Lett.*, 2006, **88**, 2004–2007.

89 P. Gutruf, C. M. Shah, S. Walia, H. Nili, A. S. Zoolfakar, C. Karnutsch, K. Kalantar-zadeh, S. Sriram and M. Bhaskaran, *NPG Asia Mater.*, 2013, **5**, e62.

90 M. Drack, I. Graz, T. Sekitani, T. Someya, M. Kaltenbrunner and S. Bauer, *Adv. Mater.*, 2015, **27**, 34–40.

91 V. Nayyar, K. Ravi-Chandar and R. Huang, *Int. J. Solids Struct.*, 2011, **48**, 3471–3483.

92 G. Shi, Z. Zhao, J. H. Pai, I. Lee, L. Zhang, C. Stevenson, K. Ishara, R. Zhang, H. Zhu and J. Ma, *Adv. Funct. Mater.*, 2016, **26**, 7614–7625.

93 Y. W. Choi, D. Kang, P. V. Pikhitsa, T. Lee, S. M. Kim, G. Lee, D. Tahk and M. Choi, *Sci. Rep.*, 2017, **7**, 40116.

94 N. N. Jason, S. J. Wang, S. Bhanushali and W. Cheng, *Nanoscale*, 2016, **8**, 16596–16605.

95 A. Kumar and G. U. Kulkarni, *J. Appl. Phys.*, 2016, **119**, 15102.

96 L. Hu, D. S. Hecht and G. Grüner, *Nano Lett.*, 2004, **4**, 2513–2517.

97 P.-C. Hsu, S. Wang, H. Wu, V. K. Narasimhan, D. Kong, H. Ryoung Lee and Y. Cui, *Nat. Commun.*, 2013, **4**, 2522.

98 P. Peng, A. Hu, H. Huang, A. P. Gerlich, B. Zhao and Y. N. Zhou, *J. Mater. Chem.*, 2012, **22**, 12997.

99 C. Gong, J. Liang, W. Hu, X. Niu, S. Ma, H. T. Hahn and Q. Pei, *Adv. Mater.*, 2013, **25**, 4186–4191.

100 B. C.-K. Tee, C. Wang, R. Allen and Z. Bao, *Nat. Nanotechnol.*, 2012, **7**, 825–832.

101 Y. Li, S. Chen, M. Wu and J. Sun, *Adv. Mater.*, 2012, **24**, 4578–4582.

102 Y. Wei, S. Chen, X. Yuan, P. Wang and L. Liu, *Adv. Funct. Mater.*, 2016, **26**, 5078–5085.

103 D.-H. Kim, R. Ghaffari, N. Lu and J. A. Rogers, *Annu. Rev. Biomed. Eng.*, 2012, **14**, 113–128.

104 E. Choi, O. Sul, S. Hwang, J. Cho, H. Chun, H. Kim and S.-B. Lee, *Nanotechnology*, 2014, **25**, 425504.

105 Y. Su, S. Wang, Y. Huang, H. Luan, W. Dong, J. A. Fan, Q. Yang, J. A. Rogers and Y. Huang, *Small*, 2015, **11**, 367–373.

106 A. M. Hussain and M. M. Hussain, *Emerging Technologies; Safety Engineering and Risk Analysis; Materials: Genetics to Structures*, ASME, 2015, vol. 14, p. V014T11A012.

107 A. Jahanshahi, M. Gonzalez, J. Van Den Brand, F. Bossuyt, T. Vervust, R. Verplancke, J. Vanfleteren and J. De Baets, *Jpn. J. Appl. Phys.*, 2013, **52**, 05DA18.

108 D.-H. Kim and J. A. Rogers, *Adv. Mater.*, 2008, **20**, 4887–4892.

109 Y. Zhu and F. Xu, *Adv. Mater.*, 2012, **24**, 1073–1077.

110 D. C. Hyun, M. Park, C. Park, B. Kim, Y. Xia, J. H. Hur, J. M. Kim, J. J. Park and U. Jeong, *Adv. Mater.*, 2011, **23**, 2946–2950.

111 S. Han, M. K. Kim, B. Wang, D. S. Wie, S. Wang and C. H. Lee, *Adv. Mater.*, 2016, **28**, 10257–10265.

112 C. Pang, G.-Y. Lee, T. Kim, S. M. Kim, H. N. Kim, S.-H. Ahn and K.-Y. Suh, *Nat. Mater.*, 2012, **11**, 795–801.

113 Y. Wang, R. Yang, Z. Shi, L. Zhang, D. Shi, E. Wang and G. Zhang, *ACS Nano*, 2011, **5**, 3645–3650.

114 J. Kim, M. Lee, H. J. Shim, R. Ghaffari, H. R. Cho, D. Son, Y. H. Jung, M. Soh, C. Choi, S. Jung, K. Chu, D. Jeon, S.-T. Lee, J. H. Kim, S. H. Choi, T. Hyeon and D.-H. Kim, *Nat. Commun.*, 2014, **5**, 5747.

115 J. a Fan, W.-H. Yeo, Y. Su, Y. Hattori, W. Lee, S.-Y. Jung, Y. Zhang, Z. Liu, H. Cheng, L. Falgout, M. Bajema, T. Coleman, D. Gregoire, R. J. Larsen, Y. Huang and J. a Rogers, *Nat. Commun.*, 2014, **5**, 3266.

116 A. Clausen, F. Wang, J. S. Jensen, O. Sigmund and J. A. Lewis, *Adv. Mater.*, 2015, **27**, 5523–5527.

117 Y. Cho, J. Shin, A. Costa, T. A. Kim, V. Kunin, J. Li, S. Y. Lee, S. Yang, H. N. Han, I.-S. Choi and D. J. Srolovitz, *Proc. Natl. Acad. Sci. U. S. A.*, 2014, **111**, 17390–17395.

118 S. Yang, Y.-C. Chen, L. Nicolini, P. Pasupathy, J. Sacks, B. Su, R. Yang, D. Sanchez, Y.-F. Chang, P. Wang, D. Schnyer, D. Neikirk and N. Lu, *Adv. Mater.*, 2015, **27**, 6423–6430.

119 T. Cheng, Y. Zhang, W.-Y. Lai and W. Huang, *Adv. Mater.*, 2015, **27**, 3349–3376.

120 B. Zhu, Z. Niu, H. Wang, W. R. Leow, H. Wang, Y. Li, L. Zheng, J. Wei, F. Huo and X. Chen, *Small*, 2014, 3625–3631.

121 Y. Wei, S. Chen, Y. Lin, Z. Yang and L. Liu, *J. Mater. Chem. C*, 2015, **3**, 9594–9602.

122 J. Seo, T. J. Lee, C. Lim, S. Lee, C. Rui, D. Ann, S.-B. Lee and H. Lee, *Small*, 2015, **11**, 2990–2994.

123 M. Segev-Bar, A. Landman, M. Nir-Shapira, G. Shuster and H. Haick, *ACS Appl. Mater. Interfaces*, 2013, **5**, 5531–5541.

124 M.-C. Hsieh, C. Kim, M. Nogi and K. Suganuma, *Nanoscale*, 2013, **5**, 9289.

125 A. Kamyshny and S. Magdassi, *Small*, 2014, **10**, 3515–3535.

126 N. N. Jason, W. Shen and W. Cheng, *ACS Appl. Mater. Interfaces*, 2015, **7**, 16760–16766.

127 L. Y. Xu, G. Y. Yang, H. Y. Jing, J. Wei and Y. D. Han, *Nanotechnology*, 2014, **25**, 55201.

128 Q. Wang, B. Su, H. Liu and L. Jiang, *Adv. Mater.*, 2014, **26**, 4889–4894.

129 X. Liao, Q. Liao, X. Yan, Q. Liang, H. Si, M. Li, H. Wu, S. Cao and Y. Zhang, *Adv. Funct. Mater.*, 2015, **25**, 2395–2401.

130 J.-W. Han, B. Kim, J. Li and M. Meyyappan, *Mater. Res. Bull.*, 2014, **50**, 249–253.

131 J.-H. Kong, N.-S. Jang, S.-H. Kim and J.-M. Kim, *Carbon*, 2014, **77**, 199–207.

132 Y. Tao, Y. Tao, L. Wang, B. Wang, Z. Yang and Y. Tai, *Nanoscale Res. Lett.*, 2013, **8**, 147.

133 C.-W. Lin, Z. Zhao, J. Kim and J. Huang, *Sci. Rep.*, 2014, **4**, 3812–3818.

134 G.-W. Huang, H.-M. Xiao and S.-Y. Fu, *Sci. Rep.*, 2015, **5**, 13971.

135 T. He, A. Xie, D. H. Reneker and Y. Zhu, *ACS Nano*, 2014, **8**, 4782–4789.

136 X. Wang, G. Li, R. Liu, H. Ding and T. Zhang, *J. Mater. Chem.*, 2012, **22**, 21824.

137 X. Wang, Y. Gu, Z. Xiong, Z. Cui and T. Zhang, *Adv. Mater.*, 2014, **26**, 1336–1342.

138 Y. Il Song, C.-M. Yang, D. Y. Kim, H. Kanoh and K. Kaneko, *J. Colloid Interface Sci.*, 2008, **318**, 365–371.

139 A. R. Rathmell and B. J. Wiley, *Adv. Mater.*, 2011, **23**, 4798–4803.

140 Y. Tang, S. Gong, Y. Chen, L. W. Yap and W. Cheng, *ACS Nano*, 2014, **8**, 5707–5714.

141 C. Hou, H. Wang, Q. Zhang, Y. Li and M. Zhu, *Adv. Mater.*, 2014, **26**, 5018–5024.

142 S. Gong, W. Schwalb, Y. Wang, Y. Chen, Y. Tang, J. Si, B. Shirinzadeh and W. Cheng, *Nat. Commun.*, 2014, **5**, 3132–3140.

143 H. L. Gao, L. Xu, F. Long, Z. Pan, Y. X. Du, Y. Lu, J. Ge and S. H. Yu, *Angew. Chem., Int. Ed.*, 2014, **53**, 4561–4566.

144 B. Y. Ahn, E. B. Duoss, M. J. Motala, X. Guo, S.-I. Park, Y. Xiong, J. Yoon, R. G. Nuzzo, J. A. Rogers and J. A. Lewis, *Science*, 2009, **323**, 1590–1593.

145 L. W. Yap, S. Gong, Y. Tang, Y. Zhu and W. Cheng, *Sci. Bull.*, 2016, **61**, 1624–1630.

146 G. C. Pidcock and M. In Het Panhuis, *Adv. Funct. Mater.*, 2012, **22**, 4790–4800.

147 Y. R. Jeong, H. Park, S. W. Jin, S. Y. Hong, S. S. Lee and J. S. Ha, *Adv. Funct. Mater.*, 2015, **25**, 4228–4236.

148 S. Ryu, P. Lee, J. B. Chou, R. Xu, R. Zhao, A. J. Hart and S. Kim, *ACS Nano*, 2015, **9**, 5929–5936.

149 R. Xu, Y. Lu, C. Jiang, J. Chen, P. Mao, G. Gao, L. Zhang and S. Wu, *ACS Appl. Mater. Interfaces*, 2014, **6**, 13455–13460.

150 X. Li, R. Zhang, W. Yu, K. Wang, J. Wei, D. Wu, A. Cao, Z. Li, Y. Cheng, Q. Zheng, R. S. Ruoff and H. Zhu, *Sci. Rep.*, 2012, **2**, 1–6.

151 S. Jung, J. H. Kim, J. Kim, S. Choi, J. Lee, I. Park, T. Hyeon and D.-H. Kim, *Adv. Mater.*, 2014, **26**, 4825–4830.

152 J. Foroughi, G. M. Spinks, S. Aziz, A. Mirabedini, A. Jeiranikhameneh, G. G. Wallace, M. E. Kozlov and R. H. Baughman, *ACS Nano*, 2016, **10**, 9129–9135.

153 J. Ge, L. Sun, F. R. Zhang, Y. Zhang, L. A. Shi, H. Y. Zhao, H. W. Zhu, H. L. Jiang and S. H. Yu, *Adv. Mater.*, 2016, **28**, 722–728.

154 Y. Wang, T. Yang, J. Lao, R. Zhang, Y. Zhang, M. Zhu, X. Li, X. Zang, K. Wang, W. Yu, H. Jin, L. Wang and H. Zhu, *Nano Res.*, 2015, **8**, 1627–1636.

155 C. S. Boland, U. Khan, C. Backes, A. O'Neill, J. McCauley, S. Duane, R. Shanker, Y. Liu, I. Jurewicz, A. B. Dalton and J. N. Coleman, *ACS Nano*, 2014, **8**, 8819–8830.

156 E. Roh, B. Hwang, D. Kim, B. Kim and N. Lee, *ACS Nano*, 2015, **9**, 6252–6261.

157 S. Lee, A. Reuveny, J. Reeder, S. Lee, H. Jin, Q. Liu, T. Yokota, T. Sekitani, T. Isoyama, Y. Abe, Z. Suo and T. Someya, *Nat. Nanotechnol.*, 2016, 1–8.

158 M. Ying, A. P. Bonifas, N. Lu, Y. Su, R. Li, H. Cheng, A. Ameen, Y. Huang and J. A. Rogers, *Nanotechnology*, 2012, **23**, 344004.

159 R. Matsuzaki and K. Tabayashi, *Adv. Funct. Mater.*, 2015, **25**, 3806–3813.

160 V. Arumugam, M. D. Naresh and R. Sanjeevi, *J. Biosci.*, 1994, **19**, 307–313.

161 Y. Cheng, R. Wang, J. Sun and L. Gao, *ACS Nano*, 2015, **9**, 3887–3895.

162 S. Hong, H. Lee, J. Lee, J. Kwon, S. Han, Y. D. Suh, H. Cho, J. Shin, J. Yeo and S. H. Ko, *Adv. Mater.*, 2015, **27**, 4744–4751.

163 I. You, B. Kim, J. Park, K. Koh, S. Shin, S. Jung and U. Jeong, *Adv. Mater.*, 2016, 6359–6364.

164 N. Luo, W. Dai, C. Li, Z. Zhou, L. Lu, C. C. Y. Poon, S. C. Chen, Y. Zhang and N. Zhao, *Adv. Funct. Mater.*, 2016, **26**, 1178–1187.

165 Y. Wang, T. Yang, J. Lao, R. Zhang, Y. Zhang, M. Zhu, X. Li, X. Zang, K. Wang, W. Yu, H. Jin, L. Wang and H. Zhu, *Nano Res.*, 2015, **8**, 1627–1636.

166 Y. Wang, L. Wang, T. Yang, X. Li, X. Zang, M. Zhu, K. Wang, D. Wu and H. Zhu, *Adv. Funct. Mater.*, 2014, **24**, 4666–4670.

167 B. Park, J. Kim, D. Kang, C. Jeong, K. S. Kim, J. U. Kim, P. J. Yoo and T. Kim, *Adv. Mater.*, 2016, **28**, 8130–8137.

168 C. Wang, X. Li, E. Gao, M. Jian, K. Xia, Q. Wang, Z. Xu, T. Ren and Y. Zhang, *Adv. Mater.*, 2016, **28**, 6640–6648.

169 D. H. Ho, Q. Sun, S. Y. Kim, J. T. Han, D. H. Kim and J. H. Cho, *Adv. Mater.*, 2016, **28**, 2601–2608.

170 B. U. Hwang, J. H. Lee, T. Q. Trung, E. Roh, D. Il Kim, S. W. Kim and N. E. Lee, *ACS Nano*, 2015, **9**, 8801–8810.

171 W. Honda, S. Harada, T. Arie, S. Akita and K. Takei, *Adv. Funct. Mater.*, 2014, **24**, 3299–3304.

172 S. Bae, Y. Lee, B. K. Sharma, H. Lee, J. Kim and J. Ahn, *Carbon*, 2013, **51**, 236–242.

173 M. D. Ho, Y. Ling, L. W. Yap, Y. Wang, D. Dong, Y. Zhao and W. Cheng, *Adv. Funct. Mater.*, 2017, 1700845.

174 S. Gong, Y. Zhao, Q. Shi, Y. Wang, L. W. Yap and W. Cheng, *Electroanalysis*, 2016, **28**, 1298–1304.

175 Z. Ma, B. Su, S. Gong, Y. Wang, L. W. Yap, G. P. Simon and W. Cheng, *ACS Sens.*, 2016, **1**, 303–311.